Narrow, fast, and "cold" mantle plumes caused by strain-weakening rheology in Earth's lower mantle

Anna Gülcher[1], Gregor Golabek[2], Marcel Thielmann[3], Maxim Dionys Ballmer[1], and Paul James Tackley[1]

[1]ETH Zurich
[2]Bayerisches Geoinstitut, University of Bayreuth
[3]University of Bayreuth

November 21, 2022

Abstract

The rheological properties of Earth's lower mantle are key for mantle dynamics and planetary evolution. The main rock-forming minerals in the lower mantle are bridgmanite (Br) and smaller amounts of ferropericlase (Fp). Previous work has suggested that the large differences in viscosity between these minerals greatly affect the bulk rock rheology. The resulting effective rheology becomes highly strain-dependent as weaker Fp minerals become elongated and eventually interconnected. This implies that strain localization may occur in Earth's lower mantle. So far, there have been no studies on global-scale mantle convection in the presence of such strain-weakening (SW) rheology. Here, we present 2D numerical models of thermo-chemical convection in spherical annulus geometry including a new strain-dependent rheology formulation for lower mantle materials, combining rheological weakening and healing terms. We find that SW rheology has several direct and indirect effects on mantle convection. The most notable direct effect is the changing dynamics of weakened plume channels as well as the formation of larger thermochemical piles at the base of the mantle. The weakened plume conduits act as lubrication channels in the mantle and exhibit a lower thermal anomaly. SW rheology also reduces the overall viscosity, notable in terms of increasing convective vigor and core-mantle boundary (CMB) heat flux. Finally, we put our results into context with existing hypotheses on the style of mantle convection and mixing. Most importantly, we suggest that the new kind of plume dynamics may explain the discrepancy between expected and observed thermal anomalies of deep-seated mantle plumes on Earth.

Narrow, fast, and "cold" mantle plumes caused by strain-weakening rheology in Earth's lower mantle

Anna J. P. Gülcher[1], G. J. Golabek[2], M. Thielmann[2], M. D. Ballmer[3], and P. J. Tackley[1]

[1]Institute of Geophysics, Department of Earth Sciences, ETH Zurich, Zurich, Switzerland
[2]Bayerisches Geoinstitut, University Bayreuth, Bayreuth, Germany
[3]UCL Earth Sciences, University College London, London, UK

Key Points:

- A new strain-weakening (SW) rheology for lower mantle materials is implemented in numerical models of global-scale mantle convection
- Such rheology causes weakening of plume conduits, forming narrow lubrication channels in the mantle through which hot material easily rises
- SW rheology in the lower mantle could explain the discrepancy between expected and observed thermal anomalies of deep mantle plumes on Earth

Corresponding author: Anna Gülcher, anna.guelcher@erdw.ethz.ch

Abstract

The rheological properties of Earth's lower mantle are key for mantle dynamics and planetary evolution. The main rock-forming minerals in the lower mantle are bridgmanite (Br) and smaller amounts of ferropericlase (Fp). Previous work has suggested that the large differences in viscosity between these minerals greatly affect the bulk rock rheology. The resulting effective rheology becomes highly strain-dependent as weaker Fp minerals become elongated and eventually interconnected. This implies that strain localization may occur in Earth's lower mantle. So far, there have been no studies on global-scale mantle convection in the presence of such strain-weakening (SW) rheology. Here, we present 2D numerical models of thermo-chemical convection in spherical annulus geometry including a new strain-dependent rheology formulation for lower mantle materials, combining rheological weakening and healing terms. We find that SW rheology has several direct and indirect effects on mantle convection. The most notable direct effect is the changing dynamics of weakened plume channels as well as the formation of larger thermochemical piles at the base of the mantle. The weakened plume conduits act as lubrication channels in the mantle and exhibit a lower thermal anomaly. SW rheology also reduces the overall viscosity, notable in terms of increasing convective vigor and core-mantle boundary (CMB) heat flux. Finally, we put our results into context with existing hypotheses on the style of mantle convection and mixing. Most importantly, we suggest that the new kind of plume dynamics may explain the discrepancy between expected and observed thermal anomalies of deep-seated mantle plumes on Earth.

Plain Language Summary

Earth's lower mantle (660-2890 km depth) controls our planet's evolution by regulating the transport of materials and heat through mantle convection. To better understand mantle convection and the evolution of Earth over billions of years, mathematical laws describing how rocks flow (viscosity) are needed. Recently, it was discovered that the deformation history of lower-mantle rocks affects the viscosity. In the lower mantle there are two main minerals: Bridgmanite (Br), which is relatively strong (high viscosity), and ferropericlase (Fp), which is relatively weak (low viscosity). When a rock containing both minerals is deformed, the weak Fp grains can form interconnected layers, lowering the overall viscosity and thus weakening the whole rock.

Here, we present prompting new results that show how mantle convection and Earth's evolution are affected by such a deformation-dependent or "strain-weakening" (SW) viscosity law, using global-scale numerical simulations of mantle convection and plate tectonics. We find that, in particular, the dynamics of hot, rising columns of mantle material (plumes) are affected by SW rheology, making them more narrow, fast, and less hot relatively to other plumes. Finally, we find that this new types of plume dynamics could be linked to several observations of mantle plumes in the Earth.

1 Introduction

Solid-state convection of the rocky, 2980-km deep mantle shapes the evolution of Earth's interior and surface over billions of years. The style of mantle convection and its temporal evolution is therefore subject to active research. At least in the lower mantle, Earth's convective system is dominated by a degree-2 pattern, with two broad, antipodal, equatorial regions of upwellings surrounded by sheets of downwellings. The convective system is further characterised by existence of several geochemically distinct (and perhaps long-term isolated) reservoirs within (e.g., Garnero & McNamara, 2008; Dziewonski et al., 2010; Torsvik et al., 2010). The two large low shear-wave velocity (LLSVP) piles in Earth's lowermost mantle spatially correlate with the two antipodal upwelling regions, and their edges seem to match with hotspot locations at the surface (Torsvik

et al., 2010; M. Li & Zhong, 2017). Since plumes can serve as an absolute reference frame for plate reconstructions (e.g., Wilson, 1963), their temporal stability at their root and any deflections during upwelling are important to establish. Even though mantle plumes are an intrinsic part of Earth's convection system, their dynamics, geometries, and fixity remain poorly understood since they were first proposed (Morgan, 1971).

To date, it is understood that mantle plumes can start as deep as the core–mantle boundary and rise all the way to the base of the lithosphere, where they sustain intraplate hotspot volcanism (Morgan, 1971). In the classical view (Howard, 1964; Richards et al., 1989), a rising mantle plume is characterized by a large head atop a narrow tail, although chemical complexities may result in deviations from such classical shapes (Farnetani & Samuel, 2005; Davaille & Vatteville, 2005; Lin & Van Keken, 2006). Plume shapes are difficult to clearly be imaged by seismic tomography due to wavefront healing (Ritsema et al., 2021). Although recent full-waveform tomography models hint at the presence of plume-like features associated with major hotspots (e.g. French & Romanowicz, 2015), ambiguity remains as to the vertical continuity of these features, as well as their shapes and stability (e.g., Wolfe et al., 2009; French & Romanowicz, 2015; Davaille & Romanowicz, 2020). Another controversy lies in the temperature excess of such mantle plumes. Excess temperatures are estimated to be 100-300 K, which is significantly lower than the expected CMB temperature difference of ∼1000 K (Boehler, 1996). While the dynamics and shapes of plumes are well studied in geodynamic models with Newtonian rheology, they strongly depend on the material properties of mantle rocks (e.g. Massmeyer et al., 2013). However, these properties, and in particular the rheology of the lower mantle, are ill-constrained.

The two main constituents of the lower mantle are bridgmanite (Br) and ferropericlase (Fp) (Hirose, Morard, et al., 2017). The viscosity of the strong mineral bridgmanite ($\eta_{\mathrm{Br}} = 10^{21}-10^{23}$ Pa·s) is several orders of magnitude larger then that of the weak ferropericlase ($\eta_{\mathrm{Fp}} = 10^{18}-10^{21}$ Pa·s) (Yamazaki & Karato, 2001; Kaercher et al., 2016). It has been suggested that for typical mantle rocks that comprise Br as well as Fp, the bulk viscosity of the rock decreases with ongoing deformation as the weaker ferropericlase crystals become elongated in the direction of strain and interconnect with each other (Girard et al., 2016) (see Fig. 1a). This experimental result was further confirmed in numerical studies on the effective rheology of a lower-mantle two-phase medium during deformation (e.g., Thielmann et al., 2020; de Montserrat et al., 2021). The weakening of the bulk rock with accumulating strain ("strain weakening") implies that deformation may localize in the lower mantle, analogous to localized shear zones in crustal rocks. Such strain localization may potentially explain the isolation of large unmixed domains in the lower mantle, which may host primordial (or "hidden") geochemical reservoirs away from regions of localized deformation (Chen, 2016; Ballmer et al., 2017; Mundl et al., 2017; Gülcher et al., 2020) (see Fig. 1b). However, the effects of strain weakening on lower-mantle convection patterns and mixing dynamics have not yet been studied using global-scale geodynamic models.

Here, we implement a macro-scale description of strain-weakening (SW) rheology in a global mantle convection model. We present 2D numerical models of thermochemical convection in a spherical annulus geometry that include a new implementation of tracking the strain ellipse at each tracer through time. We allow lower mantle materials to rheologically weaken to various degrees and investigate the effects of this rheological weakening on mantle convection dynamics. We particularly focus on the characteristics of mantle plumes in the models. We find that SW rheology has several effects on mantle dynamics, including on the *(i)* pattern of mantle flow, *(ii)* thermal evolution of the mantle, *(iii)* pile stability, and *(iv)* mantle plume dynamics. We distinguish first-order effects (directly caused by spatial viscosity variations resulting from SW rheology) and second-order effects (indirectly caused by a changing Rayleigh number caused by SW of ambient mantle), and link the results to the previously-proposed style of mantle con-

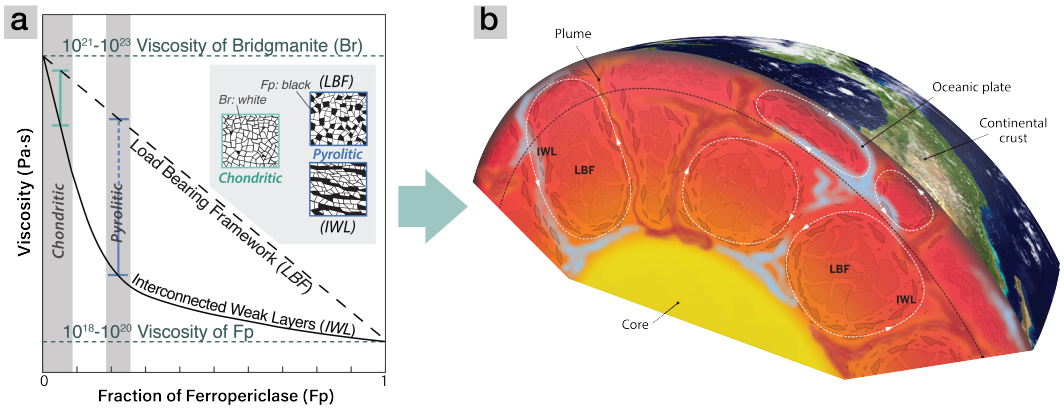

Figure 1. **(a)** Variation of the bulk viscosity of Br-Fp mixtures as a function of Fp fraction for the two end-member textures of "load-bearing framework" (LBF) and non-linear "interconnected weak layers" (IWL) (Handy, 1994). Image adapted from Ballmer et al. (2017). **(b)** Suggested mantle convection dynamics in which shear localization of weak Fp grains induces weak layers of "interconnected frameworks" (IWL) along slabs and plumes, and mixing is less efficient for the bridgmanitic "load-bearing framework" (LBF) part of the lower mantle, potentially promoting the preservation of long-lived geochemical reservoirs. From (Chen, 2016). Reprinted from Chen (2016), Copyright (2016), with permission from The American Association for the Advancement of Science (AAAS).

vection (Fig. 1b). The changing plume dynamics are of particular interest since weakened plumes could explain the discrepancy between expected and observed thermal anomalies of deep-seated mantle plumes on Earth.

2 Methods

2.1 Numerical technique and model set-up

In this study, we use the finite-volume code StagYY (Tackley, 2008) to model mantle convection in two-dimensional spherical annulus geometry (Hernlund & Tackley, 2008). The conservation equations for mass, momentum, energy and composition are solved on a staggered grid for a compressible fluid with an infinite Prandtl number. The computational domain is discretized by 1024×128 cells, in which ∼2.5 million tracers, tracking composition, temperature, and strain, are advected (20 tracers per cell). Due to vertical grid refinement near the boundary layers and near 660 km depth, the size of grid cells varies between 4 and 25 km in the vertical direction. Free-slip and isothermal boundary conditions are employed at the top and bottom boundaries, with a fixed surface temperature of 300 K and CMB temperature of 4000 K. The numerical experiments are purely bottom heated (i.e., no internal heating).

Initial mantle temperatures are calculated from an adiabat with a potential temperature of 1900 K, together with the top and bottom boundary layers, and superimposing small random temperature perturbations of ±10 K on the cell level. The resulting temperature profile is ∼300 K warmer than Earth's present-day geotherm. Such high initial mantle temperatures are applied to crudely mimic the thermal evolution of the mantle, with higher convective vigor and widespread near-surface melting in the early model evolution (e.g., Davies, 2007; Herzberg et al., 2010).

Depth [km]	**Temperature** [K]	$\triangle\rho_{\rm pc}$ [kg/m^3]	**Phase change width** [km]	γ [MPa/K]	K_0 [GPa]; K_0' [GPa/GPa]	**depth range** [km]
Olivine ($\rho_{\rm surf} = 3240$ *kg/m^3*)					163; 3.9	0-410
410	1600	180	25	+2.5	85; 3.9	410-660
660	1900	435	25	-2.5	210; 4.0	660-2740
2740	2300	61.6	25	+10	210; 4.0	2740-2890
Pyroxene-garnet ($\rho_{\rm surf} = 3080$ *kg/m^3*)					163; 3.9	0-40
40	1000	350	25	0	130; 3.9	40-300
300	1600	100	75	+1.0	85; 3.9	300-720
720	1900	350	75	+1.0	210; 4.0	720-2740
2740	2300	61.6	25	+10	210; 4.0	2740-2890

Table 1. Phase change parameters used in this study for the olivine and pyroxene-garnet systems. The table shows the depth and temperature at which a phase transition occurs; $\triangle\rho_{\rm pc}$ and γ denote the density jump across the phase transition and the Clapeyron slope, respectively. The Clapeyron slopes for these phase changes are similar to those used in previous numerical studies (e.g., Tackley et al., 2013). In the olivine system, the 410 and 660 phase changes are made discontinuous, whereas all other phase changes in all systems are defined as hyperbolic tangent functions (*tanh*) that transition between the phases across a predefined phase loop width. Finally, K_0 refers to the reference bulk modulus for the system for each individual layer (marked by the depth range), and K_0' refers to its pressure-derivative.

2.2 Treatment of mantle composition, phase changes and melting

The driving forces of mantle convection are related to rock density, which depends on temperature and composition (Nakagawa & Buffett, 2005; Tackley et al., 2013). Composition in our modelled mantle has two lithological components: harzburgite and basalt. Accordingly, each tracer carries a mechanical mixture of harzburgite and basalt. Initially, all tracers in the model carry a mechanical mixture of 80% harzburgite and 20% basalt (i.e., pyrolitic composition). Both end-member materials are treated as a mixture of olivine and pyroxene–garnet systems that undergo different solid-solid phase transitions (for details, see Nakagawa et al., 2010). Harzburgite is considered to be a mixture of 75% olivine and 25% pyroxene-garnet; basalt is considered as pure pyroxene-garnet. The resulting density profiles of harzburgite and MORB are consistent with those from (Xu et al., 2008). Compositional anomalies carried on tracers evolve from the initial state due to melt-induced differentiation: they undergo partial melting as a function of pressure, temperature and composition to sustain the formation of basaltic crust, and leaving a harzburgitic residue (for details, see Nakagawa et al., 2010).

2.3 Visco-plastic rheology

Deformation in the mantle is resisted by viscous stresses. Viscosity is temperature-, pressure-, composition- (or phase-), and strain-dependent following an Arrhenius-type viscosity law (Newtonian rheology):

$$\eta(T,P,c) = \eta_0 \cdot \lambda_{\rm c} \cdot f_{\rm w} \cdot exp\left(\frac{E_{\rm a} + P \cdot V_{\rm a}}{R \cdot T} - \frac{E_{\rm a}}{R \cdot T_0}\right) \quad (1)$$

where η_0 is the reference viscosity at zero pressure and reference temperature T_0 (= 1600 K), $E_{\rm a}$ and $V_{\rm a}$ are the activation energy and volume, respectively, T is the absolute temperature, P the pressure, and R is the gas constant (8.314 J·mol^{-1} K^{-1}). Composition-dependency is considered through prefactor $\lambda_{\rm c}$: a viscosity increase of one order of mag-

Property	Symbol	Value	Units
Mantle domain thickness	D	2890	km
Gravitational acceleration	g	9.81	m/s^2
Surface temperature	T_s	300	K
CMB temperature	T_{CMB}	4000	K
Reference viscosity	η_0	$5{\cdot}10^{20}$	Pa·s
PV viscosity contrast	λ_{pv}	10	
PPV viscosity contrast	λ_{ppv}	10^{-3}	
Reference temperature	T_0	1600	K
Initial potential temperature	$T_{0,ini}$	1900	K
Activation energy	E_a	200	kJ/mol
Activation energy - PPV	$E_{a,PPV}$	100	kJ/mol
Activation volume	V_a	$2.6{\cdot}10^{-6}$	m^3/mol
Activation volume - PPV	$V_{a,PPV}$	$1.0{\cdot}10^{-6}$	m^3/mol
Surface yield stress	τ_{yield}	30	MPa
Yield stress depth derivative	τ'_{yield}	0.01	MPa/MPa
Surface specific heat capacity	$C_{P,0}$	1200	J/(kg·K)
Surface thermal conductivity	k_0	3	W/(m·K)
Surface thermal expansivity	α_0	$3{\cdot}10^{-5}$	K^{-1}

Table 2. Physical properties used in the simulations of this study. PV = perovskite; PPV = post-perovskite. Since we solve for compressible convection, the adiabatic temperature, density, thermal conductivity, thermal expansivity, and heat capacity are pressure-dependent following a third-order Birch-Murnaghan equation of state (Tackley et al., 2013).

nitude is imposed along the 660-km depth boundary (consistent with e.g., Čížková et al., 2012), and a viscosity decrease of 10^{-3} relative to the lower mantle is imposed at post-perovskite phase transition in the lowermost mantle (as suggested by Ammann et al., 2010). By considering a linear relationship between stress and strain (Newtonian rheology), the implicit dominant deformation mechanism is diffusion creep. Note however that we consider an activation energy that is smaller than experimental constraints for the upper mantle, an approach that can account for the effects of dislocation creep (e.g., Christensen & Hofmann, 1994; van Hunen et al., 2005). With our chosen activation energy and volume, the activation enthalpy in the lower mantle varies from 262 kJ/mol to 548 kJ/mol, in line with perovskite predictions by Yamazaki and Karato (2001). An additional strain-dependency of viscosity is implemented through the weakening factor f_w (see next section). All physical and rheological parameters used in this study are listed in Table 2.

In order to obtain plate-like behavior at the surface, we assume that the material deforms plastically when a critical pressure-dependent yield stress is reached (as in Tackley, 2000a; Crameri & Tackley, 2014) (see Table 2). Plate-like behavior is evaluated using diagnostic criteria from (Tackley, 2000b): plateness p (the degree to which surface deformation is localized) and mobility m (the extent to which the lithosphere is able to move). An ideal plate tectonic style gives $p = 1$ and m close to or larger than 1.

2.4 Strain-dependent rheology

2.4.1 Finite strain

Following the finite deformation approach of (McKenzie, 1979), and building up on previous work (Xie & Tackley, 2004), the deformation tensor M is tracked on the trac-

ers, which are advected with the flow. At each time step, the velocity gradient tensor is calculated and interpolated to the position of each tracer, from which the additional deformation for that time step can be retrieved. This additional deformation is then added to the existing deformation tensor. A second-order approach is implemented following (McKenzie, 1979). This approach tracks stretching, rotation and advection in full tensor form (Fig. 2a). The eigenvectors of the matrix MM^T give the principal directions of the strain ellipse, and the square root of the eigenvalues of this matrix give the amount of strain in each direction (i.e., the semi-major and semi-minor axes a and b). The scalar (finite) strain ϵ is calculated from the semi-major and semi-minor axes of the strain ellipse (see Supporting Information Text S1 for more detail) and is defined as:

$$\epsilon = log_{10}\left(\frac{a}{b}\right) \tag{2}$$

The deformation matrix M is reset to a unit matrix when a tracer passes the depth of 660 km (i.e., the strain ellipse is reset to a circle), representing the resetting of the microstructure of the rock when it passes through a major solid-solid phase transition (e.g., Solomatov & Reese, 2008).

2.4.2 Strain weakening parametrization

Lower-mantle material is rheologically weakened following a simplified strain-dependent weakening curve (Fig. 2b):

$$f_{\mathrm{w}}(\epsilon) = 0.5 \cdot (1 + f_{\mathrm{w}}^{\max}) + 0.5 \cdot (f_{\mathrm{w}}^{\max} - 1) * \tanh\left[C \cdot (\epsilon_i - \epsilon_{\mathrm{crit}})\right] \tag{3}$$

where ϵ_{crit} is the critical strain threshold parameter (the strain at which half of the weakening has taken place, see Fig. 2b), $f_{\mathrm{w}}^{\max}$ is the maximum weakening factor (1 for no weakening), and C controls shape of strain weakening curve. How this weakening curve translates with different strain definitions is discussed in Supporting Information Text S2. As proposed by Thielmann et al. (2020) and de Montserrat et al. (2021), weakening occurs almost instantaneously as material becomes deformed (see Fig. 2b). The maximum amount of weakening ($f_{\mathrm{w}}^{\max}$) is varied between the models. For simplicity, we neglect the composition-dependency of strain weakening, as well as the anisotropy of viscosity according to the strain tensor, to establish the first-order effects of strain-weakening rheology on the lower mantle. Neglecting anisotropy assumes that the strain ellipse is well-aligned with the dominant shear direction at any finite strain.

2.4.3 Rheological healing

Processes such as diffusion-dominated annealing and/or grain growth may lead to the relaxation of deformed grains (e.g. Solomatov & Reese, 2008). For part of the models, we approximate such rheological healing by relaxing the deformation matrix (i.e., strain ellipse) towards a unity matrix (i.e., circle) with a temperature-dependent (grain growth highly depends on temperature) and pressure-dependent (diffusion is limited at higher pressures) term that may represent diffusion creep-dominated healing of microstructures. This lowers the local strain value ϵ and subsequently reduces the effective weakening that occurs. The temperature-dependency of rheological healing allows for long-term memory of deformation at cold temperatures and faster healing at deep mantle temperatures, whereas the pressure-dependency may counteract fast rheological healing at high T-P regions. Rheological healing is implemented as:

$$\frac{dM}{dt} = -H \cdot (M - I) \tag{4}$$

where H is the rheological healing rate ($H{=}\frac{1}{\tau_{\mathrm{h}}}$ with reference timescale of rheological healing τ_{h}). Accordingly, the deformation matrix M is updated as follows:

$$M_{\mathrm{new}} = M_{\mathrm{old}} \cdot exp\left(-H \cdot \mathrm{dt}\right) + I \cdot \left[1 - exp\left(-H \cdot \mathrm{dt}\right)\right] \tag{5}$$

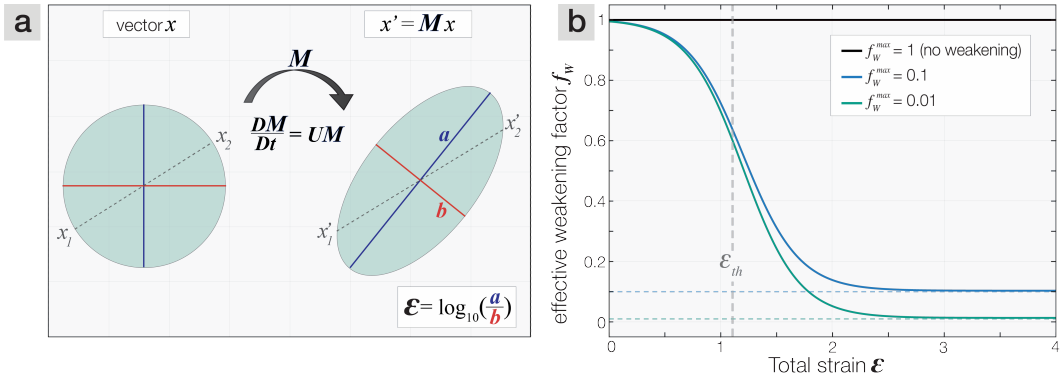

Figure 2. **(a)** The deformation matrix M relates a vector x connecting two nearby points at time t to the same vector at time zero. The time evolution of M on each tracer can be described by multiplying the velocity gradient tensor U with M (for details, see McKenzie, 1979), and M is updated at each time step on each tracer. **(b)** Weakening curve applied to all lower mantle materials in the models that explore the effect of strain-dependent rheology in the lower mantle on mantle dynamics (see Section 2.4.3, eq. 3). Input variables are $f_{\mathrm{w}}^{\mathrm{max}}$ (the maximum weakening factor f_{w}), the critical strain threshold ϵ_{th} (the strain at which half of the maximum weakening has taken place after which weakening occurs), and the shape factor C.

Where M_{new} is the updated deformation matrix, M_{old} is the deformation matrix before healing, dt is the time step in seconds and I is the unit matrix. The rheological healing rate is temperature- and pressure-dependent following:

$$H(T,P) = H_{660} \cdot exp\left\{ -\left[\frac{E_{\mathrm{a}} + (P - P_{660}) \cdot V_{\mathrm{a}}}{R \cdot T} - \frac{E_{\mathrm{a}}}{R \cdot T_{660}} \right] \right\} \tag{6}$$

where H_{660} is the reference healing rate (s^{-1}) at the top of the lower mantle (at $P = P_{660}$ and $T = T_{660}$, along the reference adiabat); this depth is chosen because weakening and healing only occur in the lower mantle. The activation energy and volume are assumed to be the same as those for diffusion creep because atomic (vacancy-) diffusion is also the mechanism by which healing occurs. More information on this rheological healing rate, the chosen reference values, and how this parametrization ultimately affects the distribution of strain in the models is described in Supporting Information Text S2.

2.5 Automated detection of mantle domains

We use the geodynamic diagnostics toolbox StagLab (Crameri, 2018) to automatically detect regional flows that are either self-driven (i.e., active) or induced (i.e., passive). Active regional flows represent mantle plumes (active upwellings) or active slabs (active downwellings). We use a new combined thermo-dynamical approach of identifying mantle plumes and slabs, which is explained in detail in Supporting Information Text S3. As a summary, active plumes and slabs are defined based on their anomalies in both temperature and radial velocity combined. Finally, the mantle diagnostics routine also detects thermochemical piles present atop the CMB (see Text S3). Using this routine, the physical properties within all different mantle domains can be separately explored.

2.6 Parameter study

In this numerical study, we vary several parameters. Most of them are related to the newly-implemented strain-weakening parameterization: we systematically vary the maximum strain weakening factor $f_{\mathrm{w}}^{\mathrm{max}}$ from 1 (no weakening) to 0.01 and the reference healing rate H_{660} in the range of 10^{-14}-10^{-16} s^{-1}, which corresponds to $\frac{1}{e}$ healing time scales of 3-300 Myr for the uppermost lower mantle. Finally, since these models including SW rheology show different final viscosity profiles, we select certain SW cases which we run again with an increased viscosity contrast between the upper and lower mantle (λ_{660} >10). The combined effect of such increased intrinsic lower-mantle viscosity and strain weakening behavior (lowering the lower mantle viscosity) gives more similar final viscosity profiles. As such, the effect of a changing Rayleigh number on mantle dynamics is eliminated and the direct effect of SW rheology can be determined.

3 Results

The relevant model parameters and output variables of all models run in this study are summarized in Supporting Information Tables S1 and S2. Videos related to the cases discussed in the text and/or highlighted in the figures can be found in the Supporting Information related to this article. All models showcased in this study show plate-like behavior according to the diagnostics of (Tackley, 2000b), and final average viscosity profiles of most models approximately agree with estimates from literature (see Supporting Information Fig. S4).

We first describe the evolution of our reference model (Section 3.1). In this model, the strain field is tracked according to the newly-implemented finite strain approach without the application of strain-dependent weakening or rheological healing. In Section (3.2), we describe the effect of the implemented strain-weakening rheology on model behavior. Two case studies are highlighted with various degrees of strain-weakening and rheological healing. Finally, in Section 3.3, we summarize the results of several case studies with various degrees of SW, but a similar final viscosity profile (Section 3.3).

3.1 Reference model evolution

The temporal evolution of our reference model (M_0), which does not include strain-weakening, is shown in Fig. 3 and in Video S1. Soon after the start of model evolution, the thermal boundary layers grow in amplitude, and after ample growth of boundary layer instabilities, a mantle overturn initiates the onset of whole-mantle convection, after which plate-tectonic behavior occurs (Table S1). The viscous flow associated with early model dynamics (at 1.0 Gyr) causes a strain field in the lower mantle that is localized in regions of buoyant, hot upwellings, and areas which are deflected by incoming, strong lithospheric drips/slabs (Fig. 3a). From the start of whole-mantle convection, the mantle gradually cools and the frequent occurrence of active mantle plumes and subducting slabs

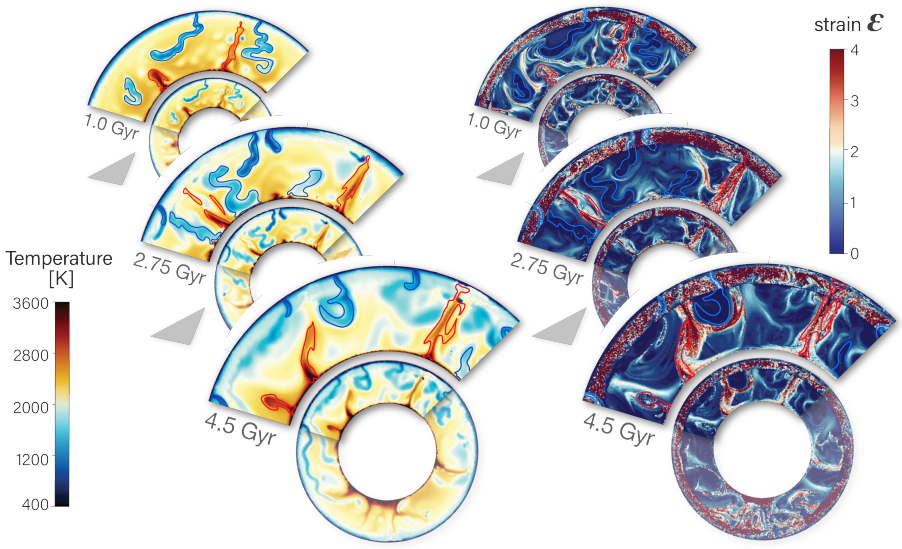

Figure 3. Temporal evolution of the reference model M_0, in which neither rheological healing nor rheological weakening is applied. Three snapshots of the temperature field (left) and strain field (right) are shown. Red outlines the edges of detected mantle plumes, and blue that of active downwellings (see Supporting Information Text S3 for their definitions).

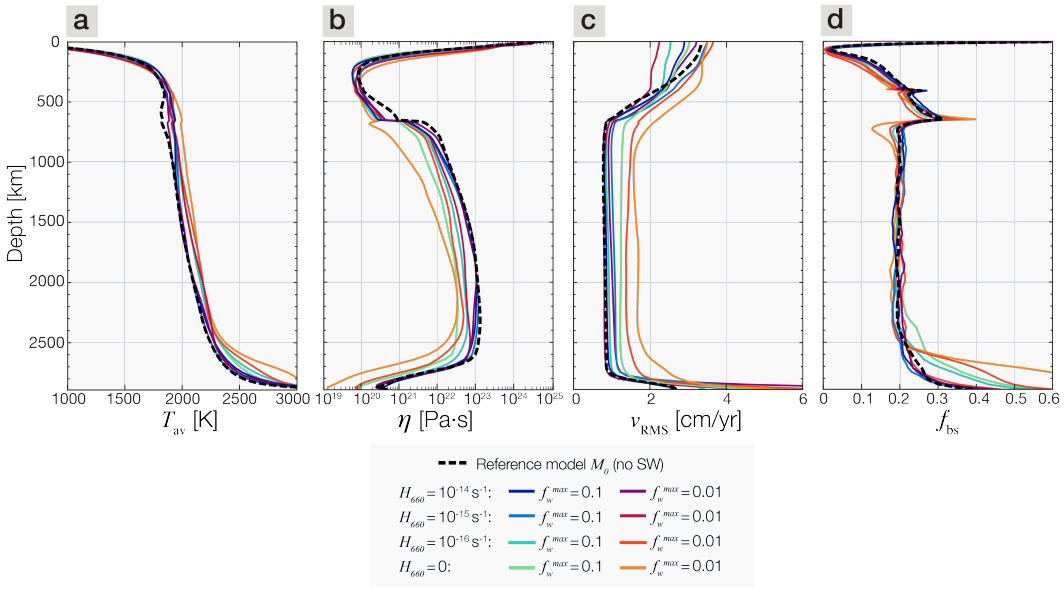

Figure 4. Radially averaged profiles of **(a)** temperature T, **(b)** viscosity η, **(c)** RMS velocity v_{RMS}, and **(d)** basalt fraction f_{bs} for all main models in this study. All radial profiles are averaged over time between 4.0 and 5.0 Gyr model time.

and active mantle plumes causes further complexity of the mantle strain pattern (Fig. 3). As the deformation history is reset at the 660 km boundary layer, small-scale strain patterns in the upper mantle are not carried into the lower mantle. Instead, strain builds up in downwelling (e.g., around slabs) and upwelling (plumes) regions of the lower mantle (Fig. 3).

The radially-averaged temperature profile displays the typical signal of efficient whole-mantle convection with boundary layers superimposed on a mostly adiabatic geotherm (Fig. 4a). The radial viscosity profile reflects the temperature- and depth-dependent rheology, as well as its compositional dependency expressed as a viscosity step towards higher values from the upper- to lower mantle (λ_{660}) (Fig. 4b). Mantle velocity is highest in the bottom ∼150 km of the lower mantle and in the upper mantle (Fig. 4c). Finally, the compositional profile shows efficient basalt segregation in a thin region on top of the CMB (tens of km) and in the mantle-transition zone (Fig. 4d).

3.2 Influence of strain-dependent rheology

In this section, we separately describe the effects of SW rheology on several key aspects of mantle convection which were introduced in Section 1. First, the effect of SW rheology on convective flow patterns is described (Section 3.2.1), followed by its effect on the thermal evolution of the mantle (Section 3.2.2), on thermochemical piles formation (Section 3.2.3), and on the dynamics of mantle plumes (Section 3.2.4).

3.2.1 Global mantle convective patterns

The radial profiles of viscosity and root mean-square (RMS) velocity of modelled mantles (Fig. 4b-c), as well as their final averages (Fig. 5b-c) show clear trends for SW rheology models. The average mantle viscosity is significantly lowered when SW rheology is applied, mostly in the lower mantle (Fig. 4b). Final convective vigor ($\sim v_{\mathrm{RMS}}$) is increased for most SW models, also mainly accommodated in the lower(most) man-

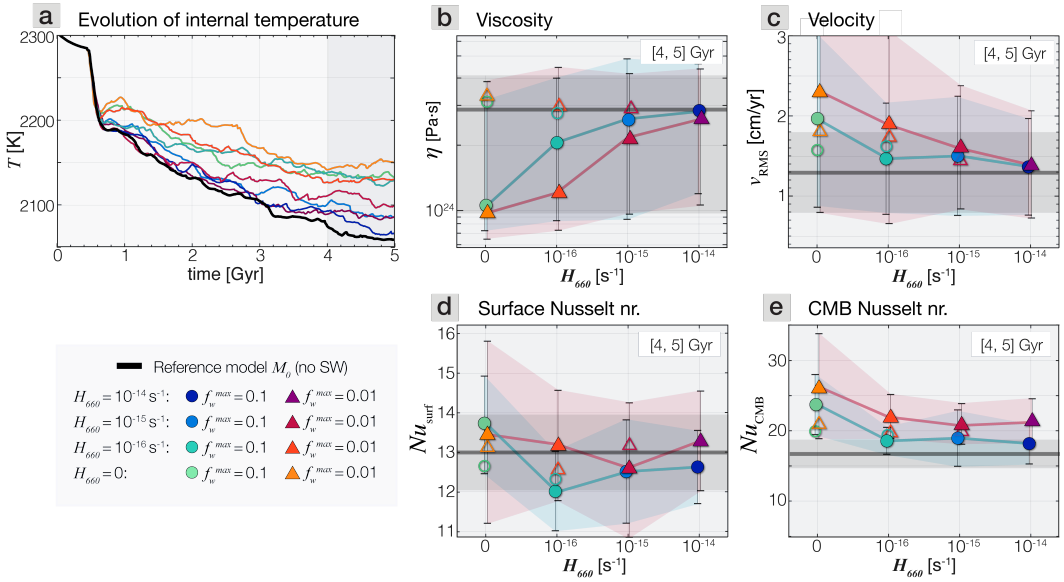

Figure 5. **(a)** Evolution of internal temperature for all main models, colors represent reference healing rate and applied weakening factor (see legend). **(b)-(e)** Selected output parameters (viscosity, velocity, surface and bottom Nu number) averaged between 4.0 and 5.0 Gyr of model time. The black line represents the reference model (neither strain-weakening nor rheological healing), with the gray shaded area showing the standard deviation. The horizontal axis represents the reference healing rate H_{660}, and the icon shape stands for the implemented strain-weakening factor $f_{\mathrm{w}}^{\mathrm{max}}$. The error bars and colored shaded areas indicate the standard-deviation of the parameter over that time period. For selected cases, outline-only symbols are also plotted, which represent the results for the additional cases with an increased viscosity jump at the 660 km discontinuity (see Section 3.3 and Supporting Information Text S4).

tle (Fig. 4c) Figure 6 shows the detected mantle domain field, i.e., passive/active up - and downwellings, of three selected models with variable degrees of SW rheology at ∼4.5 Gyr. It further shows the temporal evolution of the lateral distribution of this mantle domain field at 1800 km depth (i.e., in the middle of the lower mantle). In comparison to the reference model (Fig. 6a), SW models with an increased convective vigor show a more chaotic planform of mantle flow (Fig. 6b,c) with a larger number of small plumes present. The timescale of convection decreases with SW rheology as the convective vigor increases (overturn time $\tau \sim \frac{1}{v_{\mathrm{RMS}}}$, Miyagoshi et al. (2017)). The length-scale of convection also decreases with SW rheology as the lower mantle consists of convection cells with smaller aspect ratios, i.e., more narrow regions of up- and downwellings (Fig. 6b,c). The temporal evolution shows that the upwelling plumes in the lower mantle have shorter lifetimes than those in non-SW models. Figure 7a-c show the distribution of selected quantities in the whole mantle domain for the same three models. The v_{RMS} histograms for SW models are more skewed than that for the reference model, highlighting small domains in the mantle with very high velocities. This highlights the (albeit small) domains in which SW efficiently occurs. Interestingly, despite the changing pattern and vigor of mantle flow (described above), the statistical distribution of the age of mantle materials (defined by the time since a tracer last underwent a melting episode) in the whole mantle is similar for cases with and without SW (right panels of Fig. 7).

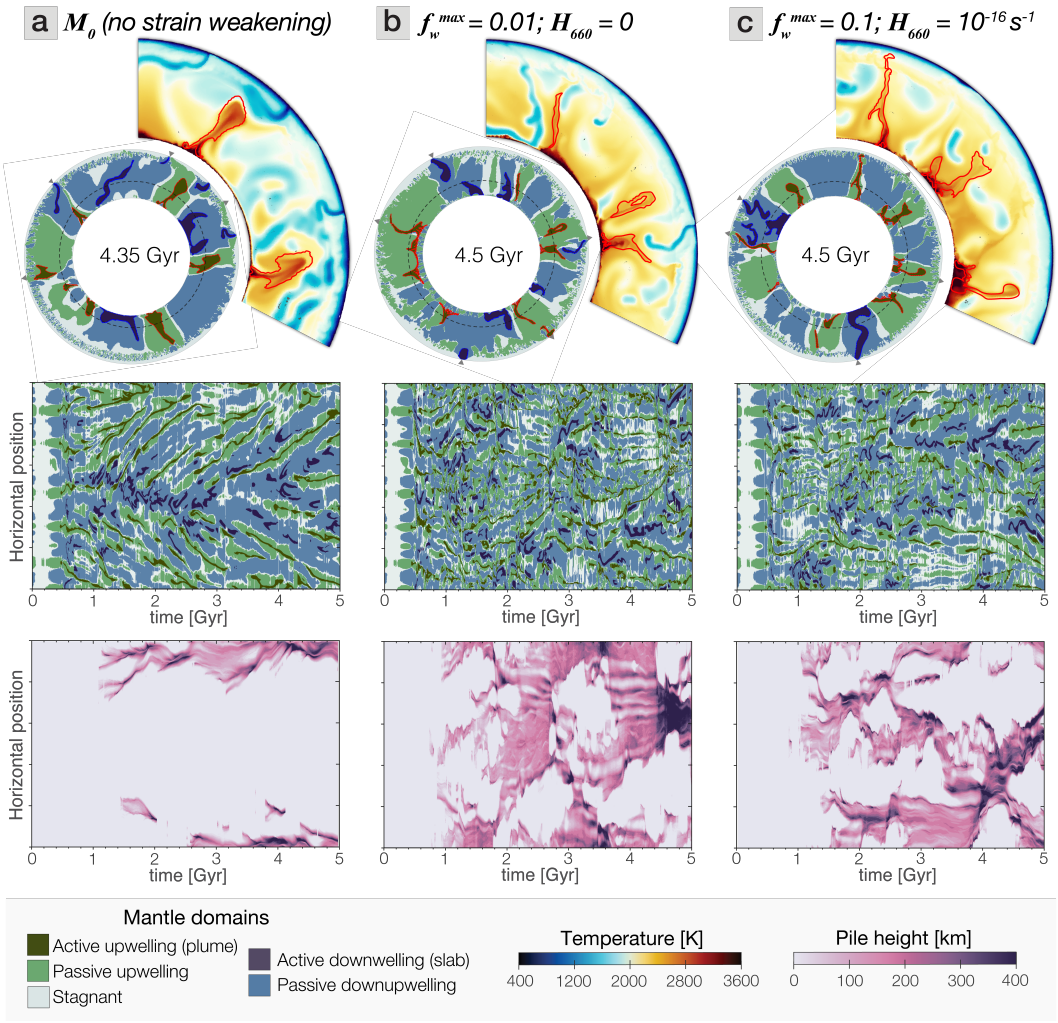

Figure 6. Top: age-of-the-Earth snapshots for three selected models showing the mantle domain field and the temperature field (a zoom-in for part of the mantle domain). Middle: temporal evolution of the lateral distribution of this field at 1800 km depth. Red outline: active mantle upwellings, blue outline: active mantle downwellings . See Section 2.5 for the definitions of the mantle domains. Bottom: temporal evolution of the lateral distribution of detected thermochemical piles atop the core-mantle boundary, color-coded according to the height of the detected pile. **(a)** Reference model: neither SW rheology nor rheological healing, **(b)** extreme case of strong strain-weakening and no rheological healing, and **(c)** model with SW rheology and healing simultaneously activated.

3.2.2 Thermal evolution

In models with SW rheology, the mantle cools down to higher final equilibrium mantle temperatures than in models with less or no SW rheology (Figs. 5a and 4c). Even with a high healing rate of $H_{660} = 10^{-14}$ s^{-1}, which causes strain in the lower mantle to heal on short geological timescales (Text S2), higher final internal temperatures are reached. This is also apparent by the relation between top and bottom Nusselt number (Nu_{top} and Nu_{bot}). Nu_{top} is not much affected by strain-weakening rheology, while Nu_{bot} is on average significantly higher for SW models (Fig. 5 d). The ratio of top/bottom

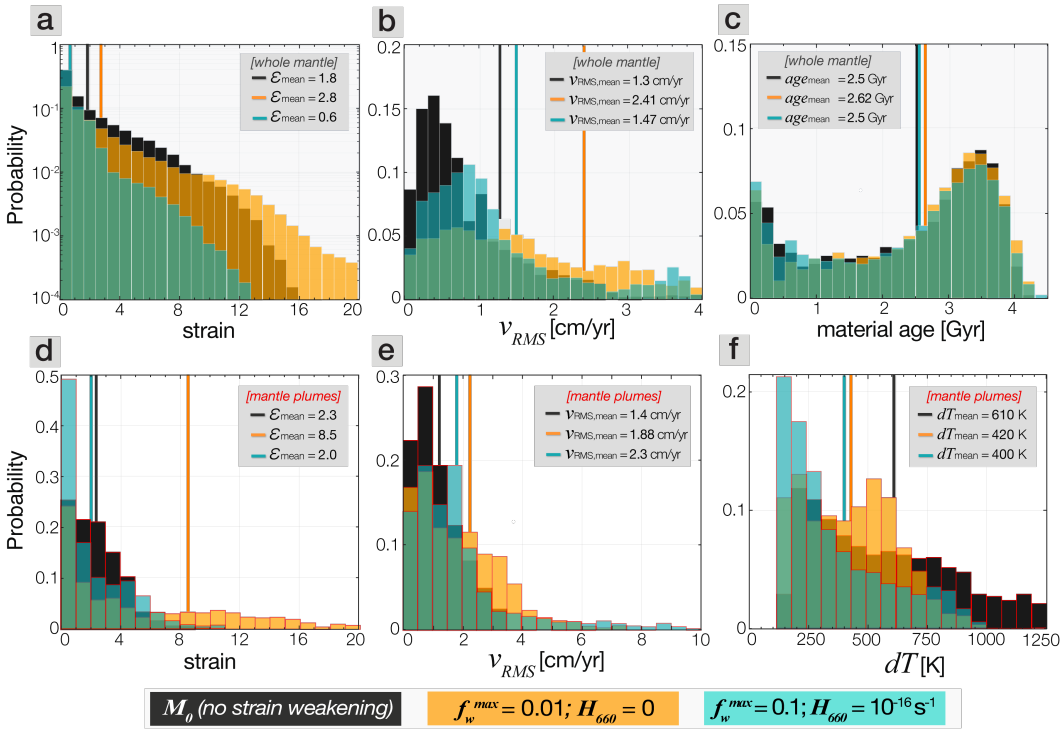

Figure 7. Histograms of selected quantities for selected models (color scale), averaged between 4.0 and 5.0 Gyr of model time. **(a)-(c)** show the distribution of the strain field (ε), the root mean-square velocity (v_{RMS}), and the material age (age) within the whole mantle domain. **(d)-(f)** show the distribution of the strain field (ε), the root mean-square velocity (v_{RMS}), and the average horizontal temperature anomaly of the material (dT) within the detected active mantle upwellings (plumes). The vertical lines represent the mean values for each histogram. Note the vertical axis of the strain histogram in panel **(a)** is logarithmic, whereas that in panel **(d)** is not.

Nusselt number is thus lowered for SW models throughout their evolution. This implies that heat is more efficiently removed from the core. In our models (constant core temperature), this causes a higher final mantle temperature in models in which SW rheology is applied. How our assumption of constant core temperature may affect these results is discussed in Section 4.4.

3.2.3 Formation of piles

Basalt segregation is most efficient in models with strong SW, because these models exhibit a low-viscosity, high-temperature mantle (see above and Figs. 4d, and Videos). Due to efficient segregation in these models, basaltic material tends to settle more efficiently in the lowermost mantle, stabilizing the formation of large thermochemical piles that cover more of the CMB (Fig. 6; Table S1). Also, the transition zone (410-660 km depth) becomes more enhanced in basaltic material ($f_{\mathrm{bs}} \approx 40\%$), while the regions around it are more depleted (Figs. 4d) (as in e.g. Ogawa, 2003; Nakagawa & Buffett, 2005; Davies, 2008; Yan et al., 2020). Moreover, the thermochemical piles are internally convecting in SW models, affecting overall heat fluxes through the mantle: due to the high intrinsic pile density, heat can build up within the piles, forming another thermal boundary layer

on top of them. Thus, these piles can act as plume generation zones in the models as active upwellings sporadically form on top of them, as well as along their edges.

3.2.4 Plume dynamics

Strain mainly localizes in hot upwellings, where material is deformed soon after model onset and subsequently subjected to weakening. Even though rheological healing partially limits such strain localisation, plume channels are still weakened in the presence of healing (see Supporting Information Text S2 and Fig. S3). According to classical thermal plume formation theories (e.g., Howard, 1964), the temperature and width of a mantle plume is related to the time over which the boundary layer grows. A thermal instability occurs when the critical boundary layer Rayleigh number is reached ($Ra_{\mathrm{local}} = Ra_{\mathrm{local,crit}}$) (Howard, 1964). If the viscosity of the material is large (low Ra_{local}), longer onset times occur, i.e., the growth rate of the instability depends inversely on the local viscosity (e.g., Howard, 1964; Griffiths & Campbell, 1990; Olson, 1990). Hot anomalies begin to separate from the layer as soon as their speed of buoyant ascent exceeds their growth rate. In our SW models, the lower viscosity of weakened plume materials would, according to the theory above, decrease the onset times of the instabilities. Since these SW instabilities have had less time to grow, there is a smaller temperature build-up compared to non-SW thermal instabilities. This precludes the growth of a wider, anomalously hot mantle plume with mushroom-shaped heads as seen in our reference model (Fig. 6a). Instead, only a narrow conduit at the center of the weakened channel remains anomalously hot, while a wider (and less hot) conduit transfers material upward. This absence of mushroom-shaped plume heads is evident for weakened plumes in both pure SW cases as well as SW + rheological healing models (Fig. 6b-c and Videos S2-S3).

The positive feedback between weakening and strain localization causes a low-viscosity channel to form in and around plumes, allowing for rapid transport of mass and heat from depth towards the surface. The typical velocities in the plume conduit tend to increase for more efficient SW (i.e., for lower $f_{\mathrm{w}}^{\mathrm{max}}$ or lower H_{660}), while the excess temperatures are lower for more efficient SW (Fig. 7, Table S2). These distinct plume dynamics caused by SW rheology are further apparent in the bottom Nusselt number (Nu_{bot}). Final Nu_{bot} is, on average, higher for models with most efficient SW rheology, linked to the thinner thermal boundary layers and higher boundary layer Rayleigh numbers (Fig. 5f). This implies that heat is more effectively lost by convection (i.e., via mantle plumes) rather than conduction. The weakened conduits are easily deflected by background flow or by incoming slabs (see Video S1). Typical timescales of plume lifetimes decrease from $\sim 500-1000$ Myr for the reference case to few 100 Myrs for the extreme SW cases (lower panels in Fig. 6).

3.3 Influence of mantle viscosity profile

Each model discussed above displays a distinct effective viscosity profile through time (Fig. 4), which, in turn, controls convective vigor and thereby strongly affects model evolution. In order to distinguish the direct (first-order) effects of SW rheology on mantle dynamics from the indirect effects of SW rheology through the radial viscosity profile (second-order), we explore additional SW cases with a higher intrinsic viscosity jump at 660 km depth (λ_{660}), such that the final viscosity profile is similar to that of the reference case. A detailed description of these results is given in Supporting Information Text S4. As a summary, these additional cases show a similar average convective vigor and thermal evolution as the reference case due to their similar viscosity profile. However, plume dynamics and the size of thermochemical piles are still affected in the same way as in the previously described SW models (see Supporting Information Text S4 and Figs. S5, S6). In fact, the localization of increased flow velocity in the narrow upwelling mantle plumes is even significantly more pronounced in these additional SW models. Moreover, thermochemical piles in the additional SW models are still substantially larger. Hence,

we conclude that SW rheology is the critical ingredient for the weakening of plume channels, their narrow shapes and relatively low thermal anomalies, as well as the formation and stabilization of large thermochemical piles. Second-order effects, such as the higher final mantle temperature, and the significantly higher average mantle flow velocities, are caused by the modification of the viscosity profile through SW.

4 Discussion

4.1 Mantle mixing and geochemical reservoirs

With an increasing convective vigor and decreasing length-scale of convection for SW models (Figs. 6 and S6), one might expect the timescale of mantle material mixing to decrease (e.g., Coltice & Schmalzl, 2006). However, in high convective-vigor SW models, basalt more easily segregates from harzburgite and thermochemical piles, which are in turn more stable over time (Section 3.2.3). Such a relation between lower mantle viscosity and more efficient basalt segregation is consistent with other studies (e.g., Yan et al., 2020). Hence, heterogeneity mixing turns out to be less efficient in models with SW rheology. Yet, the statistical distribution of mantle material age in the whole mantle is similar for all cases (Figs. 7c and S7). While a slightly higher proportion of very ancient material (>4 Ga) is preserved in SW models, a significant part of this material portion is accommodated in the thermochemical piles, which are larger and more stable in SW models. The similarity of preservation in all our models, and particularly in the convecting mantle, is contrary to earlier suggestions that SW can promote the survival of primordial materials (e.g., Girard et al., 2016; Chen, 2016). In our SW models, convection patterns are not critically stabilized over time. This result may be attributed to the lack of strain weakening in downwelling regions. Only if both upwellings and downwellings were significantly weaker than the regions in-between, we would expect efficient preservation in these in-between regions (Ballmer et al., 2017; Gülcher et al., 2020). For example, it has been proposed that grain-size reduction in cold slabs that enter the lower mantle causes local weakening (Ito & Sato, 1991; Karato et al., 2001; Yamazaki et al., 2005; Dannberg et al., 2017). Such grain-reduction weakening in combination with SW plumes may cause a style of convection dynamics more akin to previously proposed (Fig. 1b), with weakening occurring in both downwelling slabs and upwelling plumes. Future work should test if this is indeed the case.

4.2 Planetary interior evolution

Since SW rheology in the lower mantle affects CMB heat fluxes and their ratio to surface heat fluxes (Fig. 5, Table S1), it may have a substantial control on core dynamics as well as mantle cooling rates. The heat transfer from the core into the base of the mantle greatly affects the sustainability of a planetary dynamo through its control on the vigor of core convection, and the onset of inner core crystallization (Stevenson, 2003; Lay et al., 2008). Moreover, the spatial pattern of (geo-)magnetic secular variations is commonly attributed to changes in CMB heat fluxes and mantle plumes (e.g., Larson & Olson, 1991; Courtillot & Olson, 2007; Biggin et al., 2012).

Modern estimates of CMB heat flux for the Earth range from several TW up to 15 TW (e.g., Lay et al., 2008; Nakagawa, 2020), i.e., significantly lower than outcomes in our numerical models (Table S1). However, these estimates may be underestimated since they do not consider additional CMB heat flux by advection due to cold plumes (subducted plates) arriving at the base of the mantle (Labrosse, 2002). Moreover, we do not explicitly account for thermal evolution in our models (constant core temperature of 4000 K and absence of internal heating), and therefore early CMB heat flow is likely underestimated and present-day heat flux overestimated. Nevertheless, in our models, mantles with SW rheology pull out heat more efficiently from the core, which would alter planetary thermal evolution. It must be noted that if core cooling would be combined

with SW rheology, the core would cool faster which, in turn, would lower CMB heat flux and possibly final mantle temperatures. Future studies should investigate the combined effect of SW rheology and core cooling, and assess whether the indirect SW rheology effect of increasing mantle temperatures (only minor when comparing models with similar viscosity structures, see Section 3.3) still holds.

The relevance of SW rheology for (exo-)planets depends on their mineralogy and internal structure. Stars in the solar neighborhood show diverse Mg-Fe-Si compositions (Hinkel et al., 2014), with the solar composition being average in terms of Mg/Si, and near the high end of Fe/Mg (Asplund et al., 2009). Assuming stellar compositions as a proxy for rocky planet compositions (as in Spaargaren et al., 2020), planets in stellar systems with Mg/Si<1 likely have no ferropericlase in their mantle, hence no strain weakening is expected to occur. Rocky planets associated with Mg/Si$\gg$1.5 stars feature significant amounts of mantle ferropericlase, hence the material would already be weak at very small (or even zero) strain. The majority of rocky exoplanets should have an Earth-like bulk composition with 1<Mg/Si$\ll$1.5 (e.g., Spaargaren et al., 2020), where SW rheology potentially occurs in the mantle. Moreover, a recent study established the stability of a very weak B2-(Mg,Fe)O phase under extreme pressures (Coppari et al., 2021), which may dramatically affect the deep mantle rheology of Super Earths, potentially promoting SW.

4.3 Thermochemical piles

The current degree-2 pattern of Earth's mantle flow, anchored by the two antipodal LLSVP piles (Dziewonski et al., 2010), has been suggested to be a stable energy configuration from the point of view of Earth's moment of inertia and to exist for at least 200 Myrs (Burke et al., 2008; Torsvik et al., 2010, 2014; Conrad et al., 2013). Yet, this configuration is only energetically stable if LLSVPs are (much) denser than slabs, which is yet unclear (Koelemeijer et al., 2017a, 2017b; McNamara, 2019). The intrinsic high density of recycled crustal materials (basalt) already causes piles to form in our models (Fig. 6), in agreement with various geodynamical studies (Nakagawa & Buffett, 2005; Nakagawa et al., 2010; Tackley, 2012; Y. Li et al., 2014). Here, we show how SW rheology causes more efficient basalt segregation, and the formation of larger, multiple piles that cover a larger extend of the CMB (see Fig. 6 and Supporting Information Table S1).

Such thermochemical piles can act as a thermal insulator of part of the heat coming from the CMB (e.g., Lay et al., 2008; Nakagawa, 2020). Yet, the overall CMB heat flux is increased in SW rheology models. These increased values are accommodated by the much larger fluxes within the weakened plume channels (Supporting Information Table S2) as well as small-scale convective fluxes within the piles (see e.g., Fig. 6b). Moreover, plumes formed from this (secondary) thermal boundary layer have by default less heat available (Farnetani, 1997), since the temperature difference between the piles and ambient mantle is less then that between the adiabat and the CMB. This could partially explain lower temperature anomalies of these mantle plumes, although note that weakened plumes not only rise from the piles, but also from the CMB (see Figs. 6, S6, and Videos S2-S5).

4.4 Plume formation

As described in the results section (3.2.4), the differences in plume dynamics between our numerical models agree with scalings and relationships found in early classical thermal plume formation theories (e.g., Howard, 1964; Griffiths & Campbell, 1990; Olson, 1990). Thermochemical plumes, on the other hand, have different compositions, shapes and, ascent styles, as buoyancy forces of the plume are additionally affected by rheological and chemical density contrasts (Farnetani & Samuel, 2005; Davaille & Vatteville, 2005; Lin & Van Keken, 2006). Thermochemical plumes consisting of intrinsi-

cally dense material are generally wider than purely thermal plumes due to dense material that sinks back into the ascending plume (Davaille & Vatteville, 2005). Plumes in our models are of thermochemical origin, yet weakened thermochemical plume conduits are still narrow for SW rheology models.

The morphology of fully developed thermal plumes in the mantle is governed by the viscosity contrast between the plume and the mantle, and the interaction with the background mantle flow through which the plume ascends (Whitehead & Luther, 1975). The classical plume model includes a broad plume head, up to roughly thousand km in diameter, followed by a narrow plume tail, not wider than a couple of hundred kilometers (Richards et al., 1989; Sleep, 1990; Griffiths & Campbell, 1990; Davaille, 1999). In our models, plumes weakened by SW rheology substantially differ from the classical head-and-tail plume structure. Weakening of narrow conduit provides a pathway (lubrication channel) through which hot material can readily rise. In such weakened plume conduits, transport of mass and heat occurs more efficiently. Moreover, as relatively little thermal buoyancy needs to be built up to drive the plume, no head-and-tail geometry is formed. Indeed, a number of studies have shown that the conduit radius is proportional to $\eta^{1/4}$, where η is the viscosity of the hot thermal boundary layer (Griffiths & Campbell, 1990; Olson et al., 1993). Such narrow weakened plume conduits have a shorter lifetime than non-weakened plumes (Fig. 6) and they can be more easily diverted by large-scale motions and rheological contrasts in the mantle, as can be seen in the supplementary Videos.

4.5 Mantle plumes on Earth

On Earth, the mismatch between lower mantle and core adiabats implies a super-adiabatic temperature jump across the CMB of about 1000-1500 K (Jeanloz & Morris, 1986; Boehler, 1996; Lay et al., 2008). Most mantle plumes on Earth, however, are inferred to have excess temperatures of only 100-300 K (e.g., Albers & Christensen, 1996). Even when extrapolating such excess temperatures to the lower mantle, temperature anomalies of about 500 K have been inferred at the CMB (Albers & Christensen, 1996), still lower than the expected boundary layer temperature difference (Boehler, 1996). It has been argued that this mismatch is an indication for plumes rising from the top of a compositionally distinct layer at the base of the mantle (Farnetani, 1997) or for super-adiabatic rise of plumes (Bunge, 2005). Strain-weakening rheology of lower mantle materials could additionally help to explain the discrepancy between expected thermal anomalies and observed thermal anomalies of deep-seated mantle plumes, via the shorter onset times of thermal instabilities (see Section 3.2.4). On Earth, many deep-sourced plumes plumes are thought to ascend within a few tens of million years to the base of the lithosphere (e.g., Torsvik et al., 2021). From our modelled mantle plume upwelling velocities, predicted average ascent times are reduced from ∼200 Myr (for non-SW models) to an ∼110 Myr (with strain-weakening rheology). The fastest plumes in our SW models have ascent times of only 30 Myr (for 8 cm/yr rising speed), in contrast to 70 Myr for the fastest non-weakened plumes. Therefore, SW rheology could help to explain mantle plume rise speeds in the Earth's mantle. An alternative explanations for fast plume ascent involves stress-dependent non-Newtonian rheology in the lower mantle (van Keken, 1997), which is argued to produce significantly reduced plume ascent times - although in combination with larger temperature excesses because of the faster travel time (van Keken, 1997), which is not the case for weakened plumes in this study.

Even though LLSVPs have been commonly linked to plume generation (e.g., Torsvik et al., 2010), this link remains controversial. French and Romanowicz (2015) used whole-mantle seismic imaging techniques to argue for the presence of broad (not thin), quasi-vertical plumes (i.e., ∼1000 km in width) beneath many prominent hotspots. The broad plumes were inferred to be thermochemical of origin and root at the base of the mantle in patches of greatly reduced shear velocity (e.g., LLSVPs). Another line of thought is that the same seismic structures are actually a collection of poorly-resolved narrow

mantle plumes (Schubert et al., 2004; Davaille & Vatteville, 2005; Davaille & Romanowicz, 2020). In this scenario, LLSVPs are composed of plume clusters rather than being made up of stable, wide thermochemical piles with broad plume structures atop (as argued by French & Romanowicz, 2015). With state-of-the-art seismic methods, narrow mantle plumes are difficult - even impossible - to be uniquely distinguished (e.g. Hwang et al., 2011); hence further methodological advances are needed to convincingly discriminate between these two scenarios. In our models, SW rheology promotes the existence of multiple weak plume channels, that could possibly be imaged as plume clusters. Yet, in contrast to the plume bundle hypothesis (Schubert et al., 2004; Davaille & Romanowicz, 2020), such narrow, weakened plumes occur in combination with stable, thermochemical piles in the lowermost mantle. SW rheology could also help to explain faint seismically slow anomalies - or even the absence of detectable anomalies - beneath several hotspots, such as Louisville, Galapagos, and Easter (Pacific) (Davaille & Romanowicz, 2020). Finally, it must be noted that time-dependency is a key factor when interpreting present-day tomographic images of mantle upwellings. The classical image of a conduit rising from the CMB all the way to the lithosphere is only valid during part of the plume's lifetime (Davaille & Vatteville, 2005). Therefore, plumes might not be easy to detect in tomographic images, particularly if they are weakened by SW rheology, and/or deflected by mantle flow.

4.6 Future studies

Several future scientific avenues may be carried out to advance this study on the effect of SW rheology on mantle dynamics. First of all, future studies could advance our implementation by making the SW rheology composition-dependent, causing strain-dependent weakening to mainly occur in ferropericlase-enhanced regions. Subducted oceanic crust at lower mantle conditions does not contain any ferropericlase, but instead, contains much cubic $CaSiO_3$ perovskite (Hirose, Sinmyo, & Hernlund, 2017; Wicks & Duffy, 2016; Tschauner et al., 2021), which may be intrinsically weak. It is further interesting to test this composition-dependent weakening in combination with the existence of ancient bridgmanite-enhanced regions in the mid-mantle (as in Gülcher et al., 2020, 2021), which should not exhibit SW due to the absence of ferropericlase, hence promoting their preservation. Moreover, it remains to be explored how strain-dependent and grain size-dependent rheology interact with each other in the lower mantle (see Section 4.1). Finally, with the tracking of the deformation matrix in full tensor form, additional work can focus on the direction-dependency of the strain ellipse and weakening behavior and their effects on whole-mantle dynamics.

5 Conclusions

- We implemented a new strain-dependent rheology for lower mantle materials, combining rheological weakening and healing, in numerical models of global-scale mantle convection.
- Strain particularly focuses in anomalously hot regions, such as piles atop the CMB and hot mantle plumes, also when rheological healing is applied.
- SW rheology is the key ingredient for the weakening of plume channels as well as forming large thermochemical piles
- Second-order effects of SW rheology, caused by the changing mantle dynamics due to a reduction of viscosity in the lower mantle, are higher equilibrium mantle temperatures and the significantly higher average mantle flow velocities.
- Weakened mantle plumes form narrow lubrication channels in the mantle through which hot material readily rises, and they have shorter lifetimes.
- This new kind of plume dynamics may explain moderate plume excess temperatures beneath hotspots (only up to 200–300 K), given the much larger temperature difference across the core–mantle boundary (∼1000 K).

Acronyms

Myr million year
Gyr billion year
LBF load-bearing framework
IWL interconnected weak layers
CMB core-mantle boundary
LLSVP large low shear-wave velocity province
SW strain-weakening

Open Research

The open-source StagLab toolbox (Crameri, 2018) was used for detecting different mantle domains in the numerical models, creation of histogram data (Figs. 6-7, S6-S7), and creating the Videos S1-S5. The new mantle domain detection scheme (as discussed in Supporting Information Text S3) is implemented in a STAGLAB 6.0 version, and it is available on https://github.com/annaguelcher/StagLab-OS.git. Moreover, the open-source Python module StagPy (https://stagpy.readthedocs.io/en/stable/, last access: 17 July 2021) was also used for post-processing of the numerical data and production of radial and temporal profiles (Figs. 4, 5, S2, S4, and S5). The numerical code is available by reasonable request to Paul J. Tackley. All the data corresponding to the numerical experiments of this paper are too large to be placed online, but they can be requested from the corresponding author (Anna J. P. Gülcher), as can the input files for all model runs.

Supporting Information

1. Text S1 to S4
2. Figures S1 to S7
3. Tables S1 and S2
4. Videos S1 to S5

Acknowledgments

This research has mainly been supported by the ETH Zürich Research Commission (grant no. ETH-33 16-1). M. T. was supported by the Bayerisches Geoinstitut Visitor's Program. We thank Lukas Fuchs for helpful discussions related to this work, and Fabio Crameri for discussions related to visualisations and color maps. All numerical simulations were performed on ETH Zürich's Euler cluster. For 2D visualisation of the models, we used the open-source software ParaView (http://paraview.org, last access: 2 September 2021). Several perceptually uniform scientific color maps (Crameri, 2018, https://doi.org/10.5281/zenodo.1243862) were used to prevent visual distortion of the figures.

References

Albers, M., & Christensen, U. R. (1996). The excess temperature of plumes rising from the core-mantle boundary. *Geophysical Research Letters*, *23*(24), 3567–3570. doi: 10.1029/96GL03311

Ammann, M. W., Brodholt, J. P., Wookey, J., & Dobson, D. P. (2010). First-principles constraints on diffusion in lower-mantle minerals and a weak D" layer. *Nature*, *465*(7297), 462–465. Retrieved from `http://dx.doi.org/10.1038/nature09052` doi: 10.1038/nature09052

Asplund, M., Grevesse, N., Sauval, A. J., & Scott, P. (2009). The chemical compo-

652 sition of the sun. *Annual Review of Astronomy and Astrophysics*, *47*, 481–522.
653 doi: 10.1146/annurev.astro.46.060407.145222
654 Ballmer, M. D., Houser, C., Hernlund, J. W., Wentzcovitch, R. M., & Hirose, K.
655 (2017). Persistence of strong silica-enriched domains in the Earth's lower
656 mantle. *Nature Geoscience*, *10*(3), 236–240. doi: 10.1038/ngeo2898
657 Biggin, A. J., Steinberger, B., Aubert, J., Suttie, N., Holme, R., Torsvik, T. H., ...
658 Van Hinsbergen, D. J. (2012). Possible links between long-term geomagnetic
659 variations and whole-mantle convection processes. *Nature Geoscience*, *5*(8),
660 526–533. doi: 10.1038/ngeo1521
661 Boehler, R. (1996). Melting temperature of the Earth's mantle and core: Earth's
662 thermal structure. *Annual Review of Earth and Planetary Sciences*, *24*, 15–40.
663 doi: 10.1146/annurev.earth.24.1.15
664 Bunge, H. P. (2005). Low plume excess temperature and high core heat flux in-
665 ferred from non-adiabatic geotherms in internally heated mantle circulation
666 models. *Physics of the Earth and Planetary Interiors*, *153*(1-3), 3–10. doi:
667 10.1016/j.pepi.2005.03.017
668 Burke, K., Steinberger, B., Torsvik, T. H., & Smethurst, M. A. (2008). Plume Gen-
669 eration Zones at the margins of Large Low Shear Velocity Provinces on the
670 core-mantle boundary. *Earth and Planetary Science Letters*, *265*(1-2), 49–60.
671 doi: 10.1016/j.epsl.2007.09.042
672 Chen, J. (2016). Lower-mantle materials under pressure. *Science*, *351*(6269), 122–
673 123. doi: 10.1126/science.aad7813
674 Christensen, U. R., & Hofmann, A. W. (1994). Segregation of subducted oceanic
675 crust in the convecting mantle. *Journal of Geophysical Research*, *99*(B10),
676 19,867–19,884. doi: 10.1029/93jb03403
677 Čížková, H., van den Berg, A. P., Spakman, W., & Matyska, C. (2012). The vis-
678 cosity of Earth's lower mantle inferred from sinking speed of subducted litho-
679 sphere. *Physics of the Earth and Planetary Interiors*, *200-201*, 56–62. doi:
680 10.1016/j.pepi.2012.02.010
681 Coltice, N., & Schmalzl, J. (2006). Mixing times in the mantle of the early Earth
682 derived from 2-D and 3-D numerical simulations of convection. *Geophysical Re-*
683 *search Letters*, *33*(23), 5–8. doi: 10.1029/2006GL027707
684 Conrad, C. P., Steinberger, B., & Torsvik, T. H. (2013). Stability of active mantle
685 upwelling revealed by net characteristics of plate tectonics - supplementary.
686 *Nature*, *498*, 479–482. doi: 10.1038/nature
687 Coppari, F., Smith, R. F., Wang, J., Millot, M., Kim, D., Rygg, J. R., ... Duffy,
688 T. S. (2021). Implications of the iron oxide phase transition on the in-
689 teriors of rocky exoplanets. *Nature Geoscience*, *14*(3), 121–126. Re-
690 trieved from `http://dx.doi.org/10.1038/s41561-020-00684-y` doi:
691 10.1038/s41561-020-00684-y
692 Courtillot, V., & Olson, P. (2007). Mantle plumes link magnetic superchrons to
693 phanerozoic mass depletion events. *Earth and Planetary Science Letters*,
694 *260*(3-4), 495–504. doi: 10.1016/j.epsl.2007.06.003
695 Crameri, F. (2018). Geodynamic diagnostics, scientific visualisation and StagLab
696 3.0. *Geoscientific Model Development*, *11*(6), 2541–2562. doi: 10.5194/gmd-11
697 -2541-2018
698 Crameri, F., & Tackley, P. J. (2014). Spontaneous development of arcuate single-
699 sided subduction in global 3-D mantle convection models with a free sur-
700 face. *Journal of Geophysical Research: Solid Earth*, *119*(7), 5921–5942. doi:
701 10.1002/2014JB010939
702 Dannberg, J., Eilon, Z., Faul, U., Gasmöller, R., Moulik, P., & Myhill, R. (2017).
703 The importance of grain size to mantle dynamics and seismological observa-
704 tions. *Geochemistry Geophysics Geosystems*, *18*, 3034–3061. Retrieved from
705 `10.1002/2016GC006787` doi: 10.1002/2017GC006944.Received
706 Davaille, A. (1999). Two-layer thermal convection in miscible viscous fluids. *Journal*

of Fluid Mechanics, *379*, 223–253. doi: 10.1017/S0022112098003322

Davaille, A., & Romanowicz, B. (2020). Deflating the LLSVPs: Bundles of Mantle Thermochemical Plumes Rather Than Thick Stagnant "Piles". *Tectonics*, *39*(10), 1–21. doi: 10.1029/2020TC006265

Davaille, A., & Vatteville, J. (2005). On the transient nature of mantle plumes. *Geophysical Research Letters*, *32*(14), 1–4. doi: 10.1029/2005GL023029

Davies, G. F. (2007). Thermal Evolution of the Mantle. *Treatise on Geophysics*, *9*, 197–216. doi: 10.1016/B978-044452748-6.00145-0

Davies, G. F. (2008). Episodic layering of the early mantle by the 'basalt barrier' mechanism. *Earth and Planetary Science Letters*, *275*(3-4), 382–392. doi: 10.1016/j.epsl.2008.08.036

de Montserrat, A., Faccenda, M., & Pennacchionni, G. (2021). Extrinsic Anisotropy of Two-Phase Newtonian Aggregates : Fabric Characterization and Parameterization. *Journal of Geophysical Research: Solid Earth*, *126*(e2021JB022232).

Dziewonski, A. M., Lekic, V., & Romanowicz, B. A. (2010). Mantle Anchor Structure: An argument for bottom up tectonics. *Earth and Planetary Science Letters*, *299*(1-2), 69–79. doi: 10.1016/j.epsl.2010.08.013

Farnetani, C. G. (1997). Excess temperature of mantle plumes: The role of chemical stratification across D. *Geophysical Research Letters*, *24*(13), 1583–1586. doi: 10.1029/97GL01548

Farnetani, C. G., & Samuel, H. (2005). Beyond the thermal plume paradigm. *Geophysical Research Letters*, *32*(7), 1–4. doi: 10.1029/2005GL022360

French, S. W., & Romanowicz, B. (2015). Broad plumes rooted at the base of the Earth's mantle beneath major hotspots. *Nature*, *525*(7567), 95–99. doi: 10.1038/nature14876

Garnero, E. J., & McNamara, A. K. (2008). Structure and Dynamics of Earth's Lower Mantle. *Science*, *320*(5876), 626–628. doi: 10.1126/science.1148028

Girard, J., Amulele, G., Farla, R., Mohiuddin, A., & Karato, S. I. (2016). Shear deformation of bridgmanite and magnesiowüstite aggregates at lower mantle conditions. *Science*, *351*(6269), 144–147. doi: 10.1126/science.aad3113

Griffiths, R. W., & Campbell, I. H. (1990). Stirring and structure in mantle starting plumes. *Earth and Planetary Science Letters*, *99*(1-2), 66–78. doi: 10.1016/0012-821X(90)90071-5

Gülcher, A. J., Ballmer, M. D., & Tackley, P. J. (2021). Coupled dynamics and evolution of primordial and recycled heterogeneity in Earth's lower mantle. *Solid Earth*, *12*(9), 2087–2107. doi: 10.5194/se-12-2087-2021

Gülcher, A. J., Gebhardt, D. J., Ballmer, M. D., & Tackley, P. J. (2020). Variable dynamic styles of primordial heterogeneity preservation in the Earth's lower mantle. *Earth and Planetary Sciences Letters*, *536*(116160). doi: 10.1016/j.epsl.2020.116160

Handy, M. R. (1994). Flow laws for rocks containing two non-linear viscous phases : a phenomenological approach. *Journal of Structural Geology*, *16*(3), 287–301.

Hernlund, J. W., & Tackley, P. J. (2008). Modeling mantle convection in the spherical annulus. *Physics of the Earth and Planetary Interiors*, *171*(1-4), 48–54. doi: 10.1016/j.pepi.2008.07.037

Herzberg, C., Condie, K., & Korenaga, J. (2010). Thermal history of the Earth and its petrological expression. *Earth and Planetary Science Letters*, *292*(1-2), 79–88. doi: 10.1016/j.epsl.2010.01.022

Hinkel, N. R., Timmes, F. X., Young, P. A., Pagano, M. D., & Turnbull, M. C. (2014). Stellar abundances in the solar neighborhood: The hypatia catalog. *Astronomical Journal*, *148*(3). doi: 10.1088/0004-6256/148/3/54

Hirose, K., Morard, G., Sinmyo, R., Umemoto, K., Hernlund, J. W., Helffrich, G. R., & Labrosse, S. (2017). Crystallization of silicon dioxide and compositional evolution of the Earth's core. *Nature*, *543*(7643), 99–102. doi: 10.1038/nature21367

Hirose, K., Sinmyo, R., & Hernlund, J. W. (2017). Perovskite in Earth's deep interior. *Science*, *738*(November), 734–738. doi: 10.1126/science.aam8561

Howard, L. N. (1964). Thermal convection at high Rayleigh number. In H. Görtler (Ed.), *Applied mechanics. proceedings of 11th internaional congress* (pp. 1109–1115). Berlin: Springer. doi: 10.1017/s0004972700024965

Hwang, Y. K., Ritsema, J., van Keken, P. E., Goes, S., & Styles, E. (2011). Wavefront healing renders deep plumes seismically invisible. *Geophysical Journal International*, *187*(1), 273–277. doi: 10.1111/j.1365-246X.2011.05173.x

Ito, E., & Sato, H. (1991). Aseismicity in the lower mantle by superplasticity of the descending slab. *Nature*, *351*(6322), 140–141. doi: 10.1038/351140a0

Jeanloz, R., & Morris, S. (1986). Temperature distribution int he crust and mantle. *Annual Review of Earth and Planetary Sciences*, *14*, 377–415.

Kaercher, P., Miyagi, L., Kanitpanyacharoen, W., Zepeda-Alarcon, E., Wang, Y., Parkinson, D., ... Wenk, H. R. (2016). Two-phase deformation of lower mantle mineral analogs. *Earth and Planetary Science Letters*, *456*, 134–145. Retrieved from `http://dx.doi.org/10.1016/j.epsl.2016.09.030` doi: 10.1016/j.epsl.2016.09.030

Karato, S., Riedel, M. R., & Yuen, D. A. (2001). Rheological structure and deformation of subducted slabs in the mantle transition zone: Implications for mantle circulation and deep earthquakes. *Physics of the Earth and Planetary Interiors*, *127*(1-4), 83–108. doi: 10.1016/S0031-9201(01)00223-0

Koelemeijer, P., Deuss, A., & Ritsema, J. (2017a). Density structure of Earth's lowermost mantle from Stoneley mode splitting observations. *Nature Communications*, *8*(May), 1–10. Retrieved from `http://dx.doi.org/10.1038/ncomms15241` doi: 10.1038/ncomms15241

Koelemeijer, P., Deuss, A., & Ritsema, J. (2017b). Density structure of Earth's lowermost mantle from Stoneley mode splitting observations. *Nature Communications*, *8*(May), 1–10. Retrieved from `http://dx.doi.org/10.1038/ncomms15241` doi: 10.1038/ncomms15241

Labrosse, S. (2002). Hotspots, mantle plumes and core heat loss. *Earth and Planetary Science Letters*, *199*(1-2), 147–156. doi: 10.1016/S0012-821X(02)00537-X

Larson, R. L., & Olson, P. (1991). Mantle plumes control magnetic reversal frequency. *Earth and Planetary Science Letters*, *107*, 437–447.

Lay, T., Hernlund, J., & Buffett, B. A. (2008). Core – mantle boundary heat flow. *Nature Geoscience*, *1*, 25–32.

Li, M., & Zhong, S. (2017). The source location of mantle plumes from 3D spherical models of mantle convection. *Earth and Planetary Science Letters*, *478*, 47–57. Retrieved from `http://dx.doi.org/10.1016/j.epsl.2017.08.033` doi: 10.1016/j.epsl.2017.08.033

Li, Y., Deschamps, F., & Tackley, P. J. (2014). The stability and structure of primordial reservoirs in the lower mantle: Insights from models of thermochemical convection in three-dimensional spherical geometry. *Geophysical Journal International*, *199*(2), 914–930. doi: 10.1093/gji/ggu295

Lin, S. C., & Van Keken, P. E. (2006). Dynamics of thermochemical plumes: 2. Complexity of plume structures and its implications for mapping mantle plumes. *Geochemistry, Geophysics, Geosystems*, *7*(3). doi: 10.1029/2005GC001072

Massmeyer, A., Di Giuseppe, E., Davaille, A., Rolf, T., & Tackley, P. J. (2013). Numerical simulation of thermal plumes in a Herschel-Bulkley fluid. *Journal of Non-Newtonian Fluid Mechanics*, *195*, 32–45. doi: 10.1016/j.jnnfm.2012.12.004

McKenzie, D. (1979). Finite deformation during fluid flow. *Geophys. J. R. astr. Soc.*, *58*, 689–715.

McNamara, A. K. (2019). A review of large low shear velocity provinces and ultra

low velocity zones. *Tectonophysics*, *760*(August 2017), 199–220. doi: 10.1016/j.tecto.2018.04.015

Miyagoshi, T., Kameyama, M., & Ogawa, M. (2017). Extremely long transition phase of thermal convection in the mantle of massive super-Earths—. *Earth, Planets and Space*, *69*(46). doi: 10.1186/s40623-017-0630-6

Morgan, W. J. (1971). Convection plumes in the lower mantle. *Nature*, *230*(5288), 42–43. doi: 10.1038/230042a0

Mundl, A., Touboul, M., Jackson, M. G., Day, J. M., Kurz, M. D., Lekic, V., ... Walker, R. J. (2017). Tungsten-182 heterogeneity in modern ocean island basalts. *Science*, *356*(6333), 66–69. doi: 10.1126/science.aal4179

Nakagawa, T. (2020). A coupled core-mantle evolution: review and future prospects. *Progress in Earth and Planetary Science*, *7*(1). doi: 10.1186/s40645-020-00374-8

Nakagawa, T., & Buffett, B. A. (2005). Mass transport mechanism between the upper and lower mantle in numerical simulations of thermochemical mantle convection with multicomponent phase changes. *Earth and Planetary Science Letters*, *230*(1-2), 11–27. doi: 10.1016/j.epsl.2004.11.005

Nakagawa, T., Tackley, P. J., Deschamps, F., & Connolly, J. A. (2010). The influence of MORB and harzburgite composition on thermo-chemical mantle convection in a 3-D spherical shell with self-consistently calculated mineral physics. *Earth and Planetary Science Letters*, *296*(3-4), 403–412. doi: 10.1016/j.epsl.2010.05.026

Ogawa, M. (2003). Chemical stratification in a two-dimensional convecting mantle with magmatism and moving plates. *Journal of Geophysical Research*, *108*(B12). doi: 10.1029/2002jb002205

Olson, P. (1990). Hot spots, swells and mantle plumes. In M. P. Ryan (Ed.), *Magma transport and storage* (pp. 33–51). Wiley.

Olson, P., Schubert, G., & Anderson, C. (1993). Structure of axisymmetric mantle plumes. *Journal of Geophysical Research*, *98*(B4), 6829–6844.

Richards, M. A., Duncan, R. A., & Courtillot, V. E. (1989). Flood basalts and hotspot tracks: Plume heads and tails. *Science*, *246*(4926), 103–107. doi: 10.1126/science.246.4926.103

Ritsema, J., Maguire, R., Cobden, L., & Goes, S. (2021). Seismic Imaging of Deep Mantle Plumes. In H. Marquardt, M. D. Ballmer, S. Cottaar, & J. G. Konter (Eds.), *Mantle convection and surface expressions* (pp. 353–369). AGU Monograph Series 263. doi: 10.1002/9781119528609.ch14

Schubert, G., Masters, G., Olson, P., & Tackley, P. (2004). Superplumes or plume clusters? *Physics of the Earth and Planetary Interiors*, *146*(1-2), 147–162. doi: 10.1016/j.pepi.2003.09.025

Sleep, N. H. (1990). Hotspots and mantle plumes: some phenomenology. *Journal of Geophysical Research*, *95*(B5), 6715–6736. doi: 10.1029/JB095iB05p06715

Solomatov, V. S., & Reese, C. C. (2008). Grain size variations in the Earth's mantle and the evolution of primordial chemical heterogeneities. *Journal of Geophysical Research: Solid Earth*, *113*(7), 1–21. doi: 10.1029/2007JB005319

Spaargaren, R. J., Ballmer, M. D., Bower, D. J., Dorn, C., & Tackley, P. J. (2020). The influence of bulk composition on the long-term interior-atmosphere evolution of terrestrial exoplanets. *Astronomy and Astrophysics*, *643*, 1–13. doi: 10.1051/0004-6361/202037632

Stevenson, D. J. (2003). Planetary magnetic fields. *Earth and Planetary Science Letters*, *208*(1-2), 1–11. doi: 10.1016/S0012-821X(02)01126-3

Tackley, P. J. (2000a). Self-consistent generation of tectonic plates in three-dimensional mantle convection 1. pseudoplastic yielding. *Geochemistry, Geophysics, Geosystems*, *1*(1), 9–22. doi: 10.1016/S0012-821X(98)00029-6

Tackley, P. J. (2000b). Self-consistent generation of tectonic plates in time-dependent, three-dimensional mantle convection simulations 2. strain weak-

ening and asthenosphere. *Geochemistry, Geophysics, Geosystems*, *1*. doi: 10.1029/2000gc000036

Tackley, P. J. (2008). Modelling compressible mantle convection with large viscosity contrasts in a three-dimensional spherical shell using the yin-yang grid. *Physics of the Earth and Planetary Interiors*, *171*(1-4), 7–18. doi: 10.1016/j.pepi.2008.08.005

Tackley, P. J. (2012). Dynamics and evolution of the deep mantle resulting from thermal, chemical, phase and melting effects. *Earth-Science Reviews*, *110*(1-4), 1–25. doi: 10.1016/j.earscirev.2011.10.001

Tackley, P. J., Ammann, M. W., Brodholt, J. P., Dobson, D. P., & Valencia, D. (2013). Mantle dynamics in super-Earths: Post-perovskite rheology and self-regulation of viscosity. *Icarus*, *225*(1), 50–61. doi: 10.1016/j.icarus.2013.03.013

Thielmann, M., Golabek, G. J., & Marquardt, H. (2020). Ferropericlase control of lower mantle rheology: Impact of phase morphology. *Geochemistry, Geophysics, Geosystems*, *21*(e2019GC008688). doi: 10.1029/2019gc008688

Torsvik, T. H., Burke, K., Steinberger, B., Webb, S. J., & Ashwal, L. D. (2010). Diamonds sampled by plumes from the core-mantle boundary. *Nature*, *466*(7304), 352–355. Retrieved from `http://dx.doi.org/10.1038/nature09216` doi: 10.1038/nature09216

Torsvik, T. H., Svensen, H. H., Steinberger, B., Royer, D. L., Jerram, D. A., Jones, M. T., & Domeier, M. (2021). Connecting the Deep Earth and the Atmosphere. In H. Marquardt, M. D. Ballmer, S. Cottaar, & J. G. Konter (Eds.), *Mantle convection and surface expression* (pp. 413–453). Geophysical Monography Series 263. doi: 10.1002/9781119528609.ch16

Torsvik, T. H., Van Der Voo, R., Doubrovine, P. V., Burke, K., Steinberger, B., Ashwal, L. D., ... Bull, A. L. (2014). Deep mantle structure as a reference frame for movements in and on the Earth. *Proceedings of the National Academy of Sciences of the United States of America*, *111*(24), 8735–8740. doi: 10.1073/pnas.1318135111

Tschauner, O., Huang, S., Yang, S., Humayun, M., & Liu, W. (2021). Discovery of davemaoite, CaSiO 3 -perovskite, as a mineral from the lower mantle. *Science*, *894*(November), 891–894.

van Hunen, J., Zhong, S., Shapiro, N. M., & Ritzwoller, M. H. (2005). New evidence for dislocation creep from 3-D geodynamic modeling of the Pacific upper mantle structure. *Earth and Planetary Science Letters*, *238*(1-2), 146–155. doi: 10.1016/j.epsl.2005.07.006

van Keken, P. E. (1997). Evolution of starting mantle plumes: a comparison between numerical and laboratory models. *Earth and Planetary Science Letters*, *148*(97).

Whitehead, J. A., & Luther, D. S. (1975). Dynamics of laboratory diapir and plume models. *Journal of Geophysical Research*, *80*(5), 705–717. doi: 10.1029/jb080i005p00705

Wicks, J. K., & Duffy, T. S. (2016). Crystal Structures of Minerals in the Lower Mantle. *Deep Earth: Physics and Chemistry of the Lower Mantle and Core*, 69–87. doi: 10.1002/9781118992487.ch6

Wilson, J. T. (1963). *A possible origin of the Hawaiian Islands* (Vol. 51) (No. 3). doi: 10.1139/cjes-2014-0036

Wolfe, C. J., Solomon, S. C., Laske, G., Collins, J. A., Detrick, R. S., Orcutt, J. A., ... Hauri, E. H. (2009). Mantle shear-wave velocity structure beneath the Hawaiian hot spot. *Science*, *326*(5958), 1388–1390. doi: 10.1126/science.1180165

Xie, S., & Tackley, P. J. (2004). Evolution of U-Pb and Sm-Nd systems in numerical models of mantle convection and plate tectonics. *Journal of Geophysical Research: Solid Earth*, *109*(11), 1–22. doi: 10.1029/2004JB003176

Xu, W., Lithgow-Bertelloni, C., Stixrude, L., & Ritsema, J. (2008). The effect of bulk composition and temperature on mantle seismic structure. *Earth and Planetary Science Letters*, *275*(1-2), 70–79. doi: 10.1016/j.epsl.2008.08.012

Yamazaki, D., Inoue, T., Okamoto, M., & Irifune, T. (2005). Grain growth kinetics of ringwoodite and its implication for rheology of the subducting slab. *Earth and Planetary Science Letters*, *236*(3-4), 871–881. doi: 10.1016/j.epsl.2005.06.005

Yamazaki, D., & Karato, S. I. (2001). Some mineral physics constraints on the rheology and geothermal structure of Earth's lower mantle. *American Mineralogist*, *86*(4), 385–391. doi: 10.2138/am-2001-0401

Yan, J., Ballmer, M. D., & Tackley, P. J. (2020). The evolution and distribution of recycled oceanic crust in the Earth's mantle: Insight from geodynamic models. *Earth and Planetary Science Letters*, *537*(March). doi: 10.1016/j.epsl.2020.116171

Supporting Information for 'Narrow, fast, and "cold" mantle plumes caused by strain-weakening rheology in Earth's lower mantle'

Anna J. P. Gülcher[1], G. J. Golabek[2], M. Thielmann[2], M. D. Ballmer[3], and P. J. Tackley[1]

[1]Institute of Geophysics, Department of Earth Sciences, ETH Zurich, Zurich, Switzerland

[2]Bayerisches Geoinstitut, University Bayreuth, Bayreuth, Germany

[3]UCL Earth Sciences, University College London, London, UK

Contents of this file

Additional Supporting Information (Movie files uploaded separately)

This file contains Supporting Information Text S1-S4, Figures S1-S7, Tables S1 and S2, and the accompanying captions for movies S1-S5, which supplement the article 'Narrow, fast, and "cold" mantle plumes caused by strain-weakening rheology in Earth's lower mantle'.

Corresponding author: Anna Gülcher, Institute of Geophysics, Department of Earth Sciences, ETH Zurich, Zurich, Switzerland. (anna.guelcher@erdw.ethz.ch)

Text S1. Strain formulation

We have chosen to track deformation and apply weakening/healing in full tensor form, because this allows for incorporating full history-dependent deformation and strain. This is in contrast to various studies that just tracked the second invariant of strain rate (e.g., Tackley, 2000b; Fuchs & Becker, 2019). Tracking the deformation matrix (e.g. strain ellipse) also has many potentials for future research, including directional information of deformation related to mineral fabric, lattice-preferred orientation, and seismic anisotropy.

Several approaches provide a dimensionless measure of strain magnitude based on the shape of the strain ellipsoid (i.e., semi-major and -minor axes a and b, giving the maximum and minimum stretch), independently of its orientation. We chose to follow (McKenzie, 1979) by calculating the logarithmic strain ($\varepsilon_{log10} = log_{10}(a/b)$), which can be translated to the "natural strain" ($\varepsilon_{ln} = ln(a/b) = \varepsilon_{log10} \cdot ln(10)$) and the strain ellipse aspect ratio ($R = a/b = 10^{\varepsilon_{log10}}$). Figure S1 shows different projections of the same weakening profile used in this study using different finite strain definitions (horizontal axis). These different curves (same weakening behavior) highlight how the description of the temporal evolution of weakening is highly dependent on the formulation of strain applied.

Text S2. Rheological healing

Below, we detail the intermediate steps from eq. (4) to eq. (5) in the main paper.

$$\frac{dM}{dt} = -H \cdot (M - I) \tag{S1}$$

$$\frac{1}{M - I} dM = -H \cdot dt \tag{S2}$$

$$\int_{M_{\text{old}}}^{M_{\text{new}}} \frac{1}{M - I} dM = -H \cdot dt \tag{S3}$$

$$ln\left(\frac{M_{\text{new}} - I}{M_{\text{old}} - I}\right) = -H \cdot dt \tag{S4}$$

$$\frac{M_{\text{new}} - I}{M_{\text{old}} - I} = exp(-H \cdot dt) \tag{S5}$$

$$M_{\text{new}} - I = (M_{\text{old}} - I) \cdot exp(-H \cdot dt) \tag{S6}$$

$$M_{\text{new}} = M_{\text{old}} \cdot exp(-H \cdot \text{dt}) + I \cdot [1 - exp(-H \cdot \text{dt})] \tag{S7}$$

Where M_{new} is the updated deformation matrix, M_{old} is the deformation matrix before healing, dt is the time step in seconds, I is the unit matrix, and H is the rheological healing rate ($=\frac{1}{\tau_{\text{h}}}$ with reference timescale of rheological healing τ_{h}). This healing rate causes M to relax towards a unit matrix I.

Figure S2 shows healing-rate profiles based on eq. (6) in the main paper for several reference adiabats (T_0=1300, 1600 and 1900 K) as well as for the initial geotherm in our experiments.

The profiles show that rheological healing generally decreases with depth along an adiabat. On the other hand, healing is strongly temperature-dependent: healing significantly increases and decreases for temperatures hotter and cooler than the reference adiabat, respectively. The profile along the initial geotherm further shows that no significant healing is expected in the lithosphere or sinking slabs. Conversely, efficient healing should occur in anomalously hot plumes.

Final snapshots for models that differ only in the extent of imposed healing are shown in Figure S3. In these models, no strain-dependent weakening is applied. Rheological healing mainly occurs in the upper mantle ($T < 1600$ K) and relatively hot anomalies (upwellings) in the lower mantle. Cold anomalies (plates) remain unaltered by rheological healing. This affects the final strain pattern as well: for moderate healing (Fig. S3b,c), accumulated strain efficiently heals in the upper mantle as well as the narrow central conduits of the hot upwellings. Relatively warm areas around these hottest narrow conduits remain strained as they are not very efficiently healed. For fast healing (Fig. S3d), strain recovery is efficient, and only little strain is accumulated near upwellings as well as in subducted slabs in the upper mantle.

Text S3. Detection of mantle domains

We use the geodynamic diagnostics software StagLab (Crameri, 2018) to automatically detect regional flows that are either self-driven (i.e., active) or induced (i.e., passive). Active regional flows represent mantle plumes (active upwellings) or active slabs (active downwellings). Passive slab remnants in the mantle that are not actively sinking, are not detected in this routine. Many previous studies use either the temperature field (e.g., Labrosse, 2002) or the radial velocity field (e.g., Hassan et al., 2015) to detect mantle plumes in numerical mantle convection models. Yet using either such a thermal or dynamic definition does not work for our set of numerical models, as our modelled plumes significantly vary in terms of their anomalies in both temperature and radial velocity.

Here, we present our unique approach of identifying mantle plumes and slabs in our models, using a combined thermal-dynamical approach, which is newly implemented in the StagLab toolbox (Crameri, 2018), and can be found on https://github.com/annaguelcher/StagLab-OS.git. This approach analyses the temperature (T) and radial velocity field (v_z), and their horizontal residual fields T_{res} and $v_{\mathrm{z,res}}$, which are the normalised fields to the horizontal mean at each depth. These fields are combined into the residual radial heat advection, which is given as $T_{\mathrm{res}} \cdot |v_{\mathrm{z,res}}|$. Absolute values of $v_{\mathrm{z,res}}$ are used to make sure that the result is negative for cold downwellings and positive for hot upwellings. This parameter may be large for regions with an anomalously large T_{res} and/or an anomalously large $v_{\mathrm{z,res}}$ (i.e., both hot, slow upwellings and colder, fast upwellings). For the detection of plumes and slabs, the residual fields T_{res} and $T_{\mathrm{res}} \cdot |v_{\mathrm{z,res}}|$ at each time step are statistically analysed, and their percentiles $P_{\#}\{..\}$ are used for the definition

of the plume/slab thresholds. Mantle plumes are detected using the following conditions:

$$T_{\mathrm{res}} \geq P_{85}\left\{T_{\mathrm{res}}\right\} \tag{S9}$$

$$T_{\mathrm{res}} \cdot |v_{\mathrm{z,res}}| \geq P_{90}\left\{T_{\mathrm{res}} \cdot |v_{\mathrm{z,res}}|\right\} \tag{S10}$$

Where P_{85} and P_{90} are the 85^{th} and 90^{th} percentiles of the respective fields specified in the {} brackets. Slabs are detected using the following conditions:

$$T_{\mathrm{res}} \leq P_{15}\left\{T_{\mathrm{res}}\right\} \tag{S11}$$

$$T_{\mathrm{res}} \cdot |v_{\mathrm{z,res}}| \leq P_{10}\left\{T_{\mathrm{res}} \cdot |v_{\mathrm{z,res}}|\right\} \tag{S12}$$

Absolute cut-offs for minimum T_{res} and $T_{\mathrm{res}} \cdot |v_{\mathrm{z,res}}|$ are put to 50 K and ± 0.48 K cm yr^{-1} (as in Arnould et al., 2020). Once these plume and slab anomalies are located, they are checked for their connectivity using a classical image processing procedure searching for connected pixels in a matrix (Crameri, 2018, and references therein). Small anomaly areas are immediately removed (as in Crameri, 2018). Moreover, plumes in the mantle should have a minimum vertical extent ($d_z = 500$ km). The same holds for slabs in the lower mantle ($d_z = 400$ km), although this size threshold is ignored for newly-developing slab(lets) in the upper mantle, passing through a depth of 250 km.

We also detect passive up- and downwellings, that are, in contrast to the active regions defined above, flowing passively due to induced forces. These regions are defined as regions other than slabs or plumes, where the v_{z} value surpasses $1/100 \cdot \max\left(\mathrm{v_z}\right)$ (upwellings) or is lower than $1/100 \cdot \min\left(\mathrm{v_z}\right)$ (downwellings).

Finally, the mantle diagnostics routine also detects basaltic piles present at the core-mantle boundary (CMB). As internal convection usually occurs within these piles (see Results), any active upwelling (plume) detected within these piles are removed from the plume field, since this concerns a separate convecting system. The pile detection routine is based on composition and temperature: in terms of composition, pile material must consist of at least 60% of the pile must consist of basaltic material ($C_{\mathrm{bs}} \geq 0.6$). The temperature constraint is defined using the average of a mid-mantle temperature of 3000 K and the CMB temperature: $T \geq \left(3000 + T_{\mathrm{CMB}}\right)/2$ [K] (as in Schierjott et al., 2020).

Text S4. Additional SW models with similar final mantle viscosity profiles

models discussed in the main text display a distinct effective viscosity profile through time, which, in turn this strongly affects model evolution by itself. We ran five additional strain-weakening rheology cases with a higher intrinsic viscosity jump in the lower mantle ($\lambda_{660} > 10$), such that the final viscosity profiles of these cases are similar to that of the reference model M_0 (and to each other). This allows us to distinguish the direct (first-order) effects of SW

rheology on mantle dynamics from those of the radial viscosity profile (second-order effect of SW rheology). The outcomes of these additional cases are summarised in Table S2 and Figures S5-S7. Videos S4 and S5 show the time evolution of internal dynamics for two selected cases (those illustrated in Figures S6 and S7). Below follows a description of related results, ordered in a similar way as the discussion in the main text.

Global mantle convective patterns

Despite similar final mantle viscosity profile and average mantle viscosity within the ensemble of additional models and compared to the reference model M_0 (Fig. S5b), the convective vigour is still affected by SW due to localization of flow. The average values for v_{RMS} are $\sim$50% higher in the additional SW models than in the reference model case (see Table S2, Fig. S7b and Fig. 5 in the main paper). In particular, the v_{RMS} histogram is more skewed, with high values (> 2 cm/yr) for SW models, and hardly any such very high velocity domains for the reference case (Fig. S7b). Most of this increased mantle flow velocity is focused in the narrow, weakened upwelling regions (Fig. S7b,e) and Videos S4-S5). With this higher convective vigor, the patterns of mantle flow is also affected (see Fig. S6), but much less so relative to the corresponding SW rheology models with $\lambda_{660} = 10$ (see Fig. 6 in main text). While the length- and timescales of convection for our additional SW cases are much more similar to that of the reference case (M_0), SW rheology still causes the formation of narrower convection cells and more mantle plumes with shorter lifetimes (Fig. S6b-c). In terms of the distribution of the age of all mantle materials (Fig. S7c), the mean age of all mantle materials is indistinguishable between all cases, similar to our findings in the main text.

Thermal evolution

In addition to similar final mantle viscosity profiles, the additional cases also display roughly similar mantle thermal evolution and final average mantle temperatures (Fig. S5a). Top Nusselt numbers are fairly equal in all cases, whereas the bottom Nusselt numbers are still slightly increased in the additional SW rheology models (Fig. 5 in the main paper), however much less than in the related SW rheology models with $\lambda_{660} = 10$ (main paper). This strengthens our conclusion that CMB heat flux is preferentially accommodated via convection vs conduction due to SW in the lowermost mantle.

Thermochemical piles

Despite the whole-mantle viscosity being roughly equal between cases, basalt segregation is still more efficient in the additional SW rheology cases (Fig. S5c), and thermochemical piles formed in the lowermost mantle are still larger (Fig. S6; Table S1). Again, this strengthens our main conclusions.

Plume dynamics

Finally, in these additional cases, weakened mantle plumes are still significantly faster, narrower, and colder, than those in the reference case (Fig. S7d-f). In fact, the ratio of upwelling velocity

within the narrow mantle plumes over the average mantle-flow velocity is even much higher in these additional SW rheology cases compared to the corresponding SW models discussed in the main text.

Conclusions

Based on the outcomes above, we conclude that SW rheology is the critical ingredient for *(i)* weak and *(ii)* narrow plumes with *(iii)* relatively low thermal anomalies, as well as *(iv)* large and long-lived thermochemical piles. Secondary effects of SW rheology, such as on CMB heat flux and mantle cooling, are caused by its effects on mantle dynamics by increasing convective vigor (locally). At a fixed average lower-mantle viscosity, CMB heat flux and mantle thermal evolution is still affected by SW, but much less so than in our models in the main text.

Captions for Movies S1 to S5

Movie S1: Evolution of reference model M_0
Evolution of reference model M_0 (no strain weakening and no rheological healing, $\lambda_{660} = 10$) over 5 billion years of model time. The video consists of six panels, each showing a different field: **(a)** basalt fraction, **(b)** material age (time since material last underwent a melting episode), **(c)** temperature, **(d)** viscosity, **(e)** detected mantle domain field (see Text S3), and **(f)** strain field. The detailed discussion on the evolution of this model can be found in Section 3.1 of the main paper.

Movie S2: Evolution of model M_{001}
Evolution of model M_{001} ($f_{\mathrm{w}}^{\max} = 0.01$, no rheological healing, $\lambda_{660} = 10$) over 5 billion years of model time. The video consists of six panels, each showing a different field: **(a)** basalt fraction, **(b)** material age (time since material last underwent a melting episode), **(c)** temperature, **(d)** viscosity, **(e)** detected mantle domain field (see Text S3), and **(f)** strain field. In contrast to the reference model (Movie S1), the convective vigor is increased, thermochemical piles in the lowermost mantle are more stable, and mantle plumes are significantly narrower, colder, and more transient (see main paper).

Movie S3: Evolution of model $M_{01\mathrm{H16}}$
Evolution of model $M_{01\mathrm{H16}}$ ($f_{\mathrm{w}}^{\max} = 0.01$, $H_{660} = 10^{-16}$ s^{-1}, $\lambda_{660} = 10$) over 5 billion years of model time. The video consists of six panels, each showing a different field: **(a)** basalt fraction, **(b)** material age (time since material last underwent a melting episode), **(c)** temperature, **(d)** viscosity, **(e)** detected mantle domain field (see Text S3), and **(f)** strain field. Even though the strain field experienced more healing compared to pure SW models (such as Movie S2), the same type of changes in mantle flow, pile stability, and plume dynamics apply as for pure SW models (see main paper).

Movie S4: Evolution of model $M_{001\lambda}$
Evolution of model $M_{001\lambda}$ ($f_{\mathrm{w}}^{\max} = 0.01$, no rheological healing, $\lambda_{660} = 20$) over 5 billion years of model time. The video consists of six panels, each showing a different field: **(a)** basalt fraction, **(b)** material age (time since material last underwent a melting episode), **(c)** temperature, **(d)** viscosity, **(e)** detected mantle domain field (see Text S3), and **(f)** strain field. Even though SW rheology operates in the modelled lower mantle, the model shows a similar thermal evolution and final viscosity profile as the reference model M_0 (see Fig. S5) due to the increased viscosity jump in the lower-mantle (λ_{660}). Strain localization still occurs in mantle plumes and thermochemical piles, and their dynamics are different than those in the reference model (see Text S4).

Movie S5: Evolution of model $M_{01\mathrm{H16}\lambda}$
Evolution of model $M_{01\mathrm{H16}\lambda}$ ($f_{\mathrm{w}}^{\max} = 0.01$, no rheological healing, $\lambda_{660} = 20$) over 5 billion years of model time. The video consists of six panels, each showing a different field: **(a)** basalt fraction, **(b)** material age (time since material last underwent a melting episode), **(c)** tempera-

ture, **(d)** viscosity, **(e)** detected mantle domain field (see Text S3), and **(f)** strain field. Even though SW rheology operates in the modelled lower mantle, the model shows a similar thermal evolution and final viscosity profile as the reference model M_0 (see Fig. S5) due to the increased viscosity jump in the lower-mantle (λ_{660}). Strain localization still occurs in mantle plumes and thermochemical piles, and their dynamics are different than those in the reference model (see Text S4).

References

Arnould, M., Coltice, N., Flament, N., & Mallard, C. (2020). Plate tectonics and mantle controls on plume dynamics. *Earth and Planetary Science Letters*, *547*, 116439. Retrieved from https://doi.org/10.1016/j.epsl.2020.116439 doi: 10.1016/j.epsl.2020.116439

Crameri, F. (2018). Geodynamic diagnostics, scientific visualisation and StagLab 3.0. *Geoscientific Model Development*, *11*(6), 2541–2562. doi: 10.5194/gmd-11-2541-2018

Forte, A. M., & Mitrovica, J. X. (1996). New inferences of mantle viscosity from joint inversion of long-wavelength mantle convection an post-glacial rebound data. *Geophysical Research Letters*, *23*(10), 1147–1150.

Fuchs, L., & Becker, T. W. (2019). Role of strain-dependent weakening memory on the style of mantle convection and plate boundary stability. *Geophysical Journal International*, *218*(1), 601–618. doi: 10.1093/gji/ggz167

Hassan, R., Flament, N., Gurnis, M., Bower, D. J., & Müller, D. (2015). Provenance of plumes in global convection models. *Geochemistry Geophysics Geosystems*, *16*(1), 267–300. Retrieved from https://doi.org/10.1002/2014GC005606 doi: 10.1002/2014GC005684.Key

Labrosse, S. (2002). Hotspots, mantle plumes and core heat loss. *Earth and Planetary Science Letters*, *199*(1-2), 147–156. doi: 10.1016/S0012-821X(02)00537-X

Lau, H. C., Mitrovica, J. X., Austermann, J., Crawford, O., Al-Attar, D., & Latychev, K. (2016). Inferences of mantle viscosity based on ice age data sets: Radial structure. *Journal of Geophysical Research: Solid Earth*, *121*(10), 6991–7012. doi: 10.1002/2016JB013043

McKenzie, D. (1979). Finite deformation during fluid flow. *Geophys. J. R. astr. Soc.*, *58*, 689–715.

Mitrovica, J. X., & Forte, A. M. (2004). A new inference of mantle viscosity based upon joint inversion of convection and glacial isostatic adjustment data. *Earth and Planetary Science Letters*, *225*(1-2), 177–189. doi: 10.1016/j.epsl.2004.06.005

Peltier, W. R. (1996). Mantle viscosity and ice-age ice sheet topography. *Science*, *273*(5280), 1359–1364. doi: 10.1126/science.273.5280.1359

Schierjott, J., Rozel, A., & Tackley, P. J. (2020). On the self-regulating effect of grain size evolution in mantle convection models: Application to thermochemical piles. *Solid Earth*, *11*(3), 959–982. doi: 10.5194/se-11-959-2020

Steinberger, B., & Calderwood, A. R. (2006). Models of large-scale viscous flow in the Earth's mantle with constraints from mineral physics and surface observations. *Geophysical Journal International*, *167*(3), 1461–1481. doi: 10.1111/j.1365-246X .2006.03131.x

Steinberger, B., & Holme, R. (2008). Mantle flow models with core-mantle boundary constraints and chemical heterogeneities in the lowermost mantle. *Journal of Geophysical Research: Solid Earth*, *113*(5), 1–16. doi: 10.1029/2007JB005080

Tackley, P. J. (2000a). Self-consistent generation of tectonic plates in three-dimensional mantle convection 1. pseudoplastic yielding. *Geochemistry, Geophysics, Geosystems*, *1*(1), 9–22. doi: 10.1016/S0012-821X(98)00029-6

Tackley, P. J. (2000b). Self-consistent generation of tectonic plates in time-dependent, three-dimensional mantle convection simulations 2. strain weakening and asthenosphere. *Geochemistry, Geophysics, Geosystems*, *1*. doi: 10.1029/2000gc000036

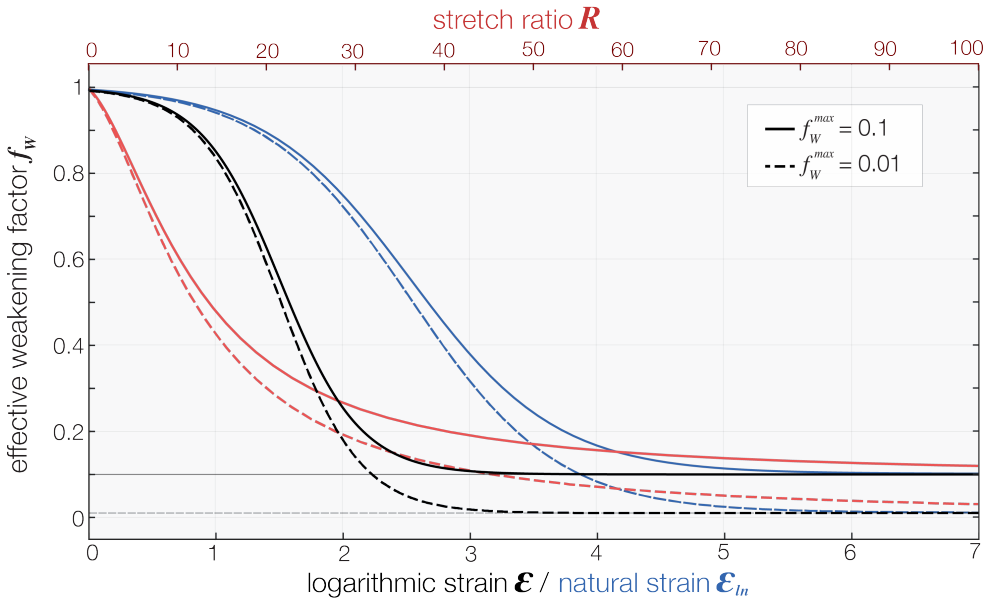

Figure S1. Same weakening curve employing different projections: (black) As a function of logarithmic strain ($\varepsilon = log_{10}(a/b)$ - as used in the main text), (blue) natural strain ($\varepsilon_{ln} = ln(a/b)$) and (red) the stretch ratio ($R = a/b$).

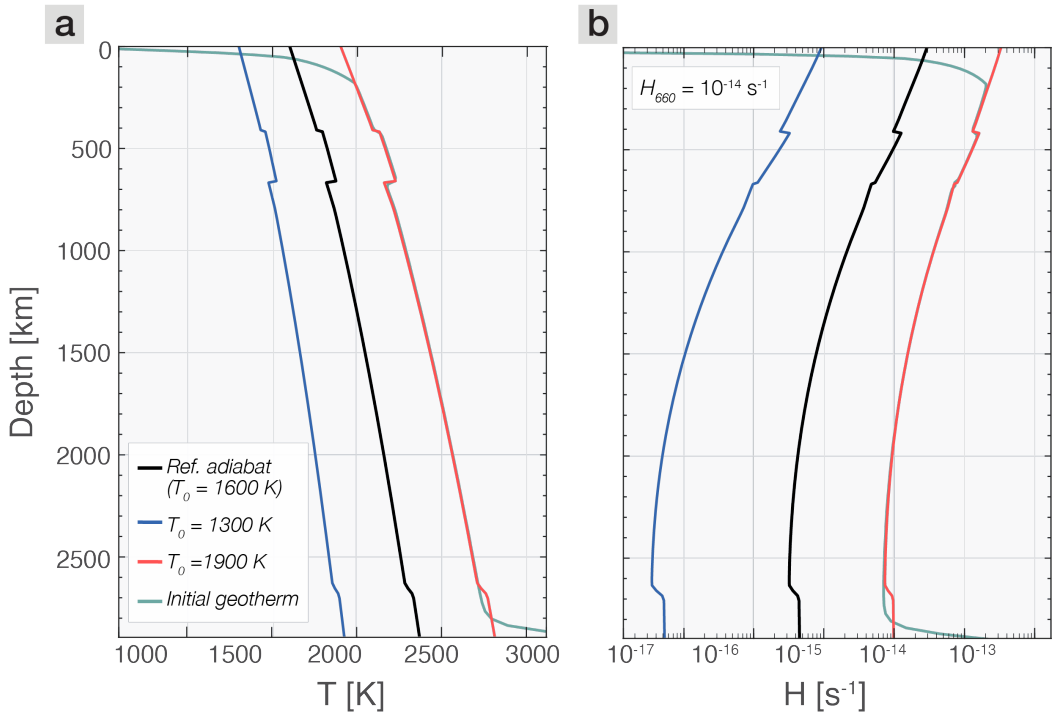

Figure S2. **(a)** reference adiabat with $T_0 = 1600$ K, and shifted +300 K and −300 K, and the initial geotherm of the model. **(b)** resulting healing rate profiles based on eq. (6) in the main text, with reference healing rate at 660 km depth: $H_{660} = 10^{-15}$ s^{-1}.

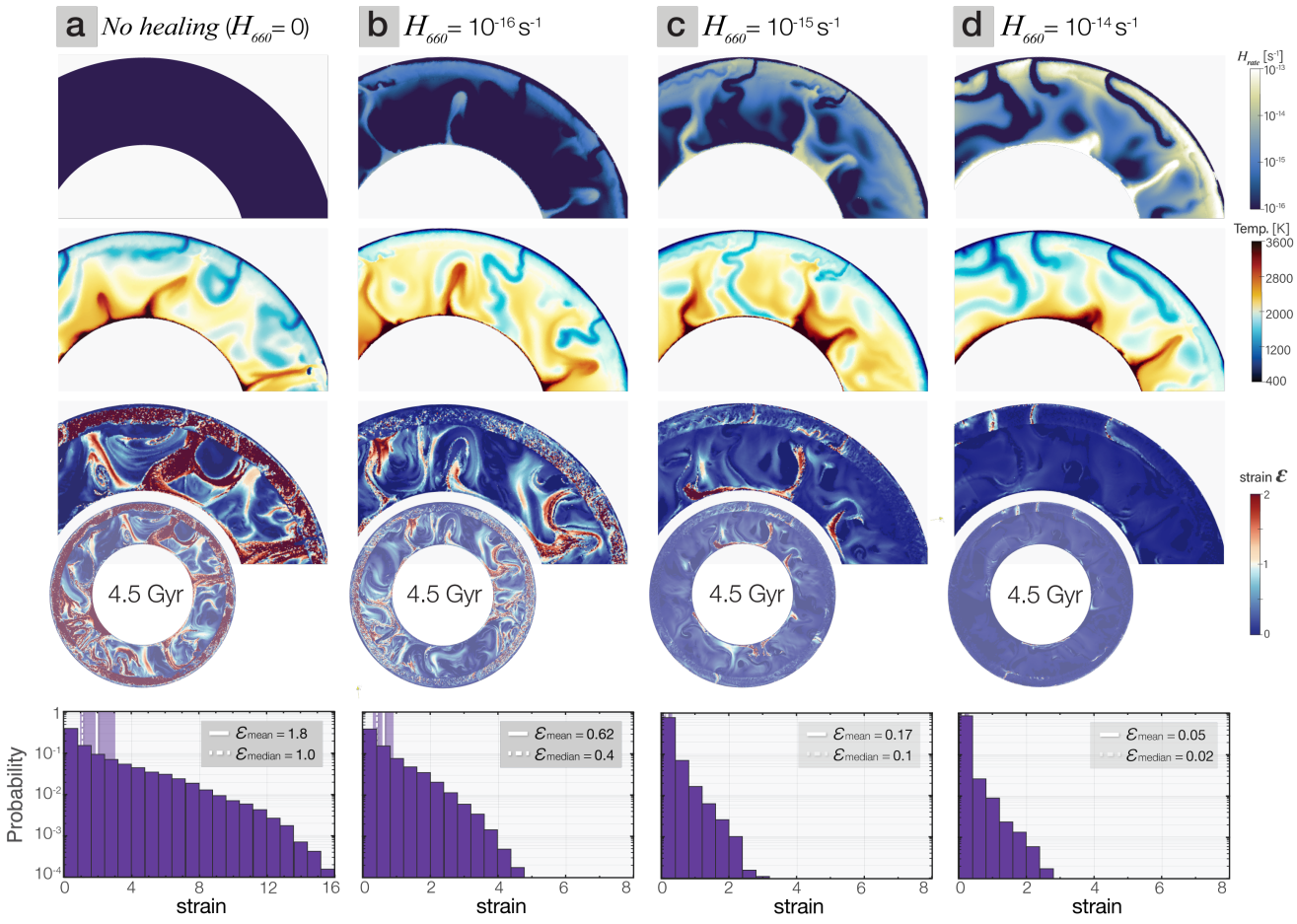

Figure S3. Final snapshots of models with, from left to right, an increasing rheological healing rate of strain. **(a)** shows the reference model (zero strain weakening and zero rheological healing). Panels **(b-d)** show models with no strain weakening rheology, but increasing healing rate (H_{660}) values: 10^{-16} s^{-1}, 10^{-15} s^{-1}, and 10^{-14} s^{-1}, respectively. These different healing rates affect the strain field significantly. Since no strain weakening is applied in these models, the differences in healing rates do not affect model evolution. Top row: healing rate, second row: temperature, third row: strain, fourth row: strain histogram (vertical lines represent the mean and median values for each histogram).

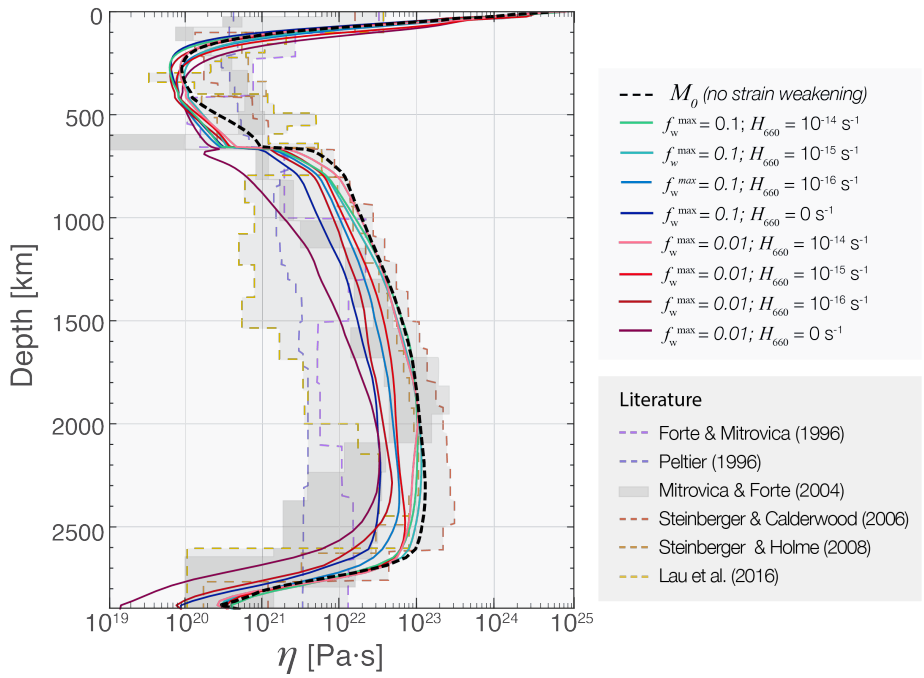

Figure S4. Solid lines: final averaged viscosity profiles of all main models in this study. Dotted lines: several radial viscosity profiles for Earth from previous studies, inferred from post-glacial rebound data (Peltier, 1996; Lau et al., 2016); joint post-glacial rebound and convection data (Forte & Mitrovica, 1996; Mitrovica & Forte, 2004); joint mineral physics and surface observations (Steinberger & Calderwood, 2006); joint mineral physics, surface observations, and convection data (Steinberger & Holme, 2008).

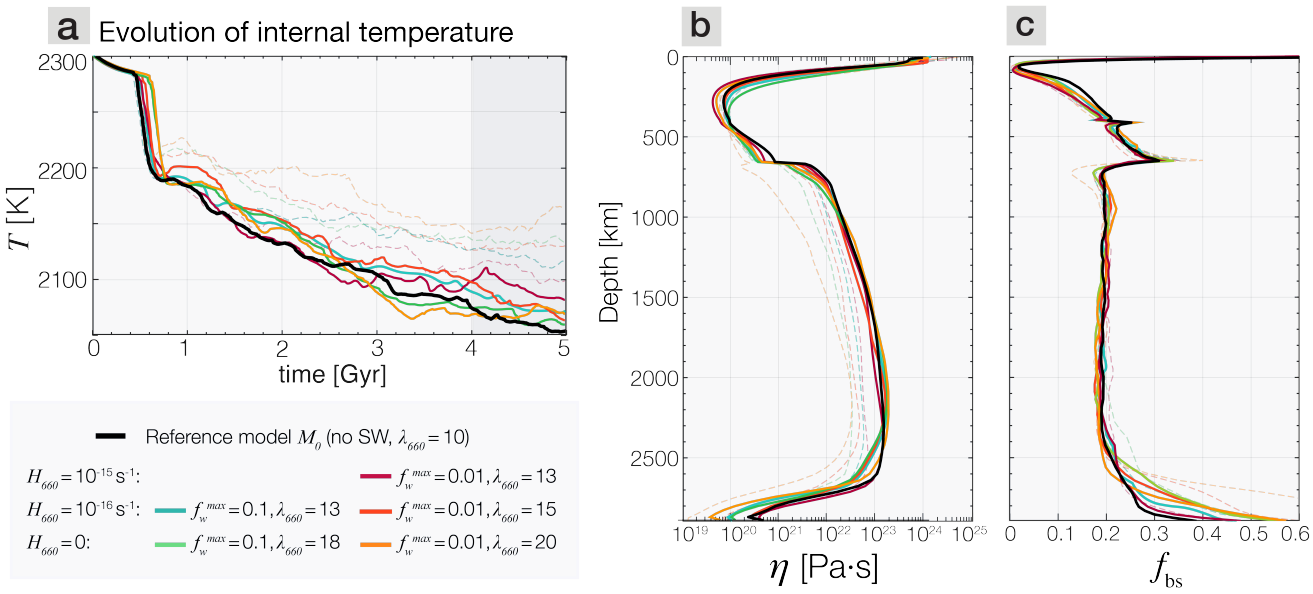

Figure S5. **a)** Temporal evolution of internal temperature for reference model case (black line) and additional SW cases (color-coded) with variable weakening + healing scenarios and an increased lower mantle viscosity jump. **(b)** All of these cases display a similar final lower mantle viscosity profile. Panel **(c)** shows the basalt radial profiles. The radial profiles are averaged between 4 and 5 Gyr. The dashed lines are the SW models corresponding to the additional cases but with λ_{660}=10.

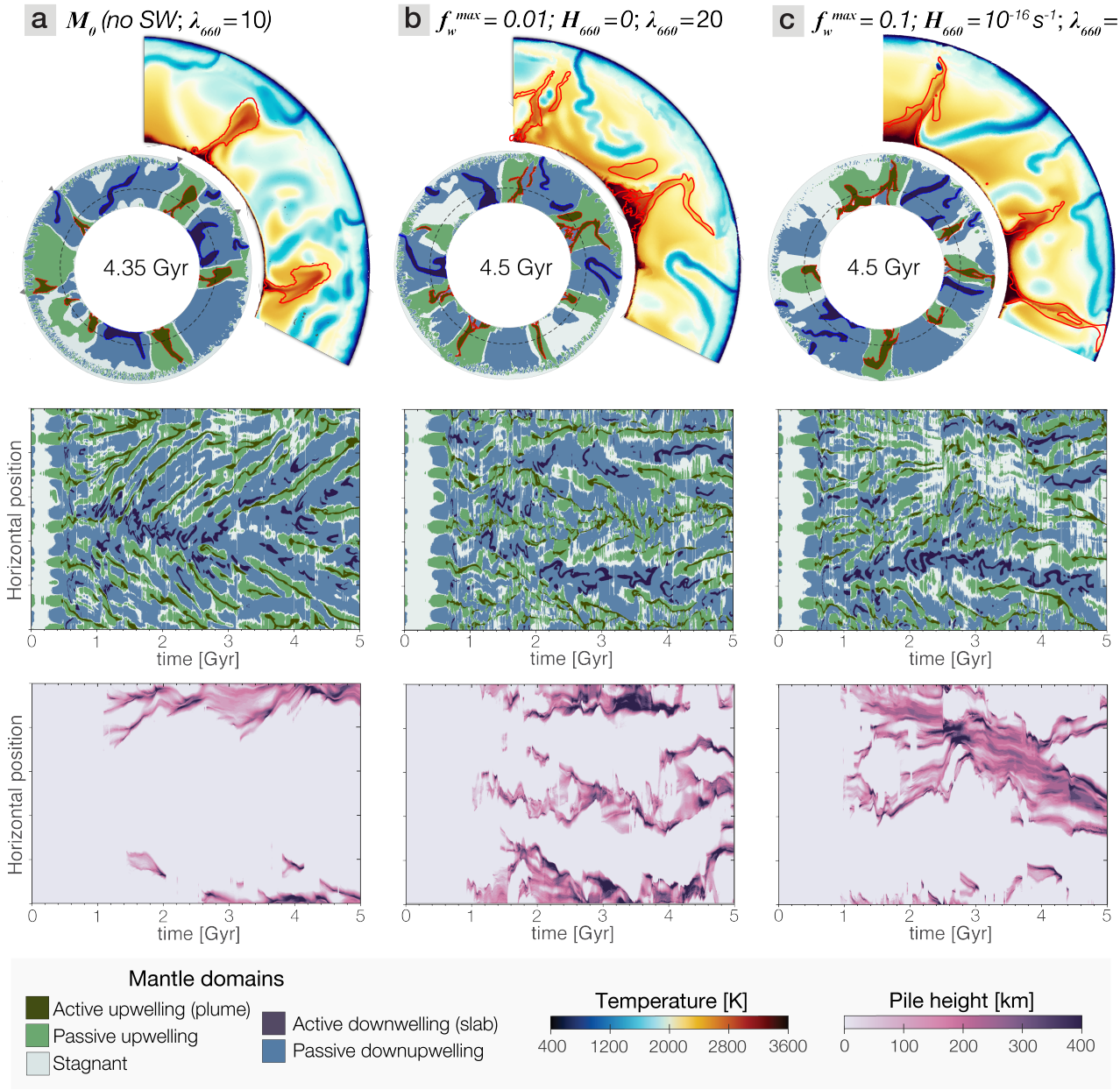

Figure S6. Top: age-of-the-Earth snapshots for three selected models showing the mantle domain field. Red outline: active mantle upwellings, blue outline: active mantle downwellings. Zoom-ins show the temperature field. Bottom: temporal evolution of the lateral distribution of the mantle domain field at 1800 km depth. See Section 2.5 in the main text for the definitions of the mantle domains. Bottom: temporal evolution of the lateral distribution of detected thermochemical piles atop the core-mantle boundary, color-coded according to the height of the detected pile. **(a)** Reference model: neither SW rheology nor rheological healing. **(b)** Additional case with strain-weakening, no rheological healing and an increased viscosity jump at the 660 boundary (λ_{660}). **(c)** Additional case with SW rheology and healing simultaneously activated, as well as an increased λ_{660}. See Text S4 for more details regarding these additional cases.

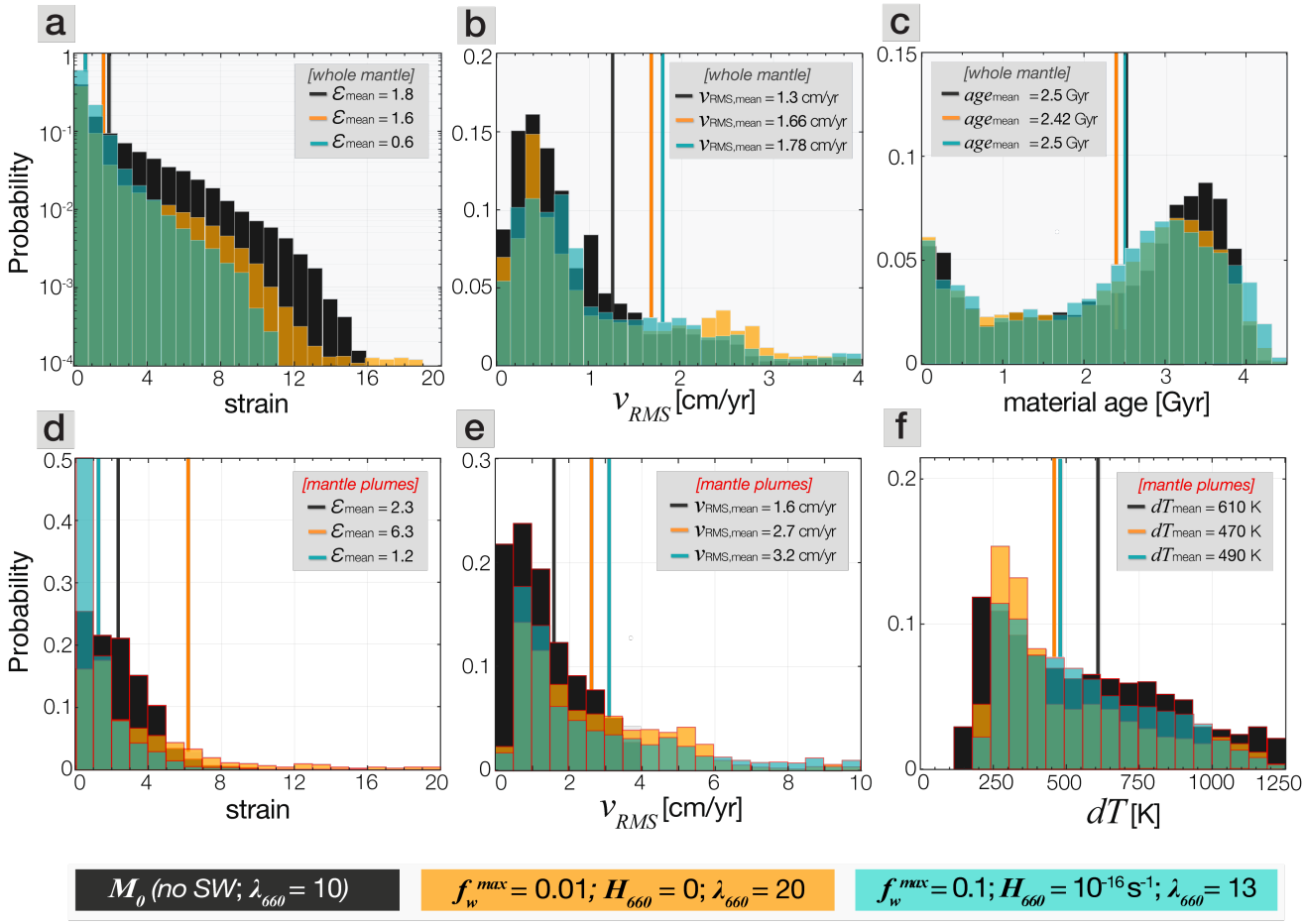

Figure S7. Histograms of selected quantities for selected models: the reference model M_0 (black) and two additional cases with variable combinations of strain-weakening and healing plus an increased viscosity jump (λ_{660}) at the 660 km discontinuity (orange, blue). The colour scheme corresponds to that in Figure 6 in the main text, with the difference being the higher viscosity jump in the additional cases explored here. See Text S4 for details. **(a-c)** Distribution of the strain field, the root mean-square velocity, and the material age within the whole mantle domain. **(d-f)** Distribution of the strain field, the root mean-square velocity, and the average horizontal temperature anomaly of the material within the detected active mantle upwellings (plumes). The vertical lines represent the mean values for each histogram.

Table S1. Model parameter summary and output quantities of all models run in this study, time-averaged between 4.0 and 5.0 Gyr of model evolution. Subscript $_{\mathrm{m}}$ stands for the average in the whole mantle (weighted by the volume of each cell). p and m stand for Plateness and Mobility, respectively (Tackley, 2000a). ϵ represents strain, T the temperature, v_{RMS} the root-mean-square velocity, Nu_{top} and Nu_{bot} the top and bottom Nusselt number, respectively. F_{top} and F_{bot} are the top and bottom heat flux, age is the age of the mantle material (time since it last underwent a melting episode), and $Pile_{\mathrm{vol}}$ is the mantle volume percentage occupied by detected thermochemical piles.

Model	$f_{\mathrm{w}}^{\mathrm{max}}$	H_{660} [s^{-1}]	λ_{660}	p	m	ε_{m}	T_{m} [K]	η_{m} [Pa·s]	$v_{\mathrm{RMS,m}}$ [cm/yr]	Nu_{bot}	Nu_{top}	F_{top} [TW]	F_{bot} [TW]	age [Gyr]	$Pile_{\mathrm{vol}}$ [$\mathrm{vol}_{\mathrm{mantle}}$%]
M_0	0	0	10	0.96	1.8	1.6	2042	$1.2{\cdot}10^{24}$	1.31	17	13	22	28	2.5	0.6
M_{01}	0.1	0	10	0.97	1.6	2.2	2108	$1.0{\cdot}10^{24}$	1.97	24	13.8	25	40	2.5	1.7
M_{001}	0.01	0	10	0.97	1.3	2.8	2132	$9.2{\cdot}10^{23}$	2.41	27	13.6	25	44	2.6	2.2
$M_{01\mathrm{H}16}$	0.1	10^{-16}	10	0.97	1.6	0.6	2102	$1.1{\cdot}10^{24}$	1.47	18	12	23	31	2.5	1.4
$M_{001\mathrm{H}16}$	0.01	10^{-16}	10	0.97	1.6	0.8	2104	$1.0{\cdot}10^{24}$	1.90	23	13.2	25	40	2.6	1.8
$M_{01\mathrm{H}15}$	0.1	10^{-15}	10	0.97	1.6	0.4	2063	$1.2{\cdot}10^{24}$	1.50	20	12.6	23	36	2.4	1.2
$M_{001\mathrm{H}15}$	0.01	10^{-15}	10	0.97	1.6	0.6	2090	$1.1{\cdot}10^{24}$	1.68	21	12.6	24	34	2.5	1.4
$M_{01\mathrm{H}14}$	0.1	10^{-14}	10	0.97	1.6	0.2	2072	$1.2{\cdot}10^{24}$	1.34	18	12.7	23	31	2.5	0.8
$M_{001\mathrm{H}14}$	0.01	10^{-14}	10	0.97	1.5	0.3	2065	$1.2{\cdot}10^{24}$	1.38	22	13.3	25	38	2.6	1.1
$M_{01\lambda}{}^{*}$	0.1	0	18	0.97	1.6	1.6	2060	$1.2{\cdot}10^{24}$	1.56	20	12.7	24	35	2.5	1.0
$M_{001\lambda}{}^{*}$	0.01	0	20	0.97	1.4	1.8	2061	$1.2{\cdot}10^{24}$	1.82	21	13	25	40	2.4	1.1
$M_{01\mathrm{H}16\lambda}{}^{*}$	0.1	10^{-16}	13	0.97	1.4	0.6	2077	$1.2{\cdot}10^{24}$	1.63	19	12.6	23	29	2.5	1.0
$M_{001\mathrm{H}16\lambda}{}^{*}$	0.01	10^{-16}	15	0.97	1.4	0.7	2080	$1.2{\cdot}10^{24}$	1.77	18	13.2	23	33	2.4	1.0
$M_{001\mathrm{H}15\lambda}{}^{*}$	0.01	10^{-15}	13	0.97	1.5	0.4	2093	$1.2{\cdot}10^{24}$	1.48	20	12.3	23	31	2.5	0.8

* Additional cases with $\lambda_{660} > 10$, see Text S4 and Figures S5-S7.

Table S2. Summary of average quantities within detected mantle plumes ($_{\mathrm{pl}}$) in the models, time-averaged between 4.0 and 5.0 Gyr of model evolution. ϵ stands for the strain, dT the horizontal temperature anomaly, v_{RMS} the root-mean-square velocity, F the heat flux carried by the plumes at 1800 km depth (middle of the lower mantle), and T_{660} the temperature of the plumes detected at 660 km depth (just below the mantle transition zone).

Model	$f_{\mathrm{w}}^{\mathrm{max}}$	H_{660} [s^{-1}]	λ_{660}	$\varepsilon_{\mathrm{pl}}$	dT_{pl} [K]	$v_{\mathrm{RMS,pl}}$ [cm/yr]	F_{pl} [TW]	$T_{pl,660}$ [K]
M_0	0	0	10	2.3	610	1.4	18	1905
M_{01}	0	0.1	10	6.2	400	1.71	22	1991
M_{001}	0	0.01	10	8.5	420	1.88	24	2075
$M_{01\mathrm{H16}}$	0.1	10^{-16}	10	2.0	400	2.3	26	2031
$M_{001\mathrm{H16}}$	0.01	10^{-16}	10	2.4	431	2.5	27	2057
$M_{01\mathrm{H15}}$	0.1	10^{-15}	10	1.6	508	1.6	22	1977
$M_{001\mathrm{H15}}$	0.01	10^{-15}	10	1.9	447	1.8	24	1996
$M_{01\mathrm{H14}}$	0.1	10^{-14}	10	1.4	560	1.5	21	1949
$M_{001\mathrm{H14}}$	0.01	10^{-14}	10	1.6	522	1.7	22	1968
$M_{01\lambda}{}^*$	0.1	0	10	5.2	502	2.3	26	1985
$M_{001\lambda}{}^*$	0.01	0	10	6.3	470	2.7	29	2016
$M_{01\mathrm{H16}\lambda}{}^*$	0.1	10^{-16}	10	1.2	490	3.2	25	2009
$M_{001\mathrm{H16}\lambda}{}^*$	0.01	10^{-16}	10	1.4	460	3.3	24	2029
$M_{001\mathrm{H15}\lambda}{}^*$	0.01	10^{-15}	10	1.0	500	3.0	23	1993

* Additional cases with $\lambda_{660} > 10$, see Text S4 and Figures S5-S7.